


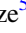










The Mass Relations between Supermassive Black Holes and Their Host Galaxies at $1 < z < 2$ with *HST*-WFC3

Xuheng Ding^{1,2} , John Silverman^{3,4} , Tommaso Treu¹ , Andreas Schulze⁵ , Malte Schramm⁵, Simon Birrer¹ , Daeseong Park⁶ , Knud Jahnke⁷ , Vardha N. Bennert⁸ , Jeyhan S. Kartaltepe⁹ , Anton M. Koekemoer¹⁰ , Matthew A. Malkan¹ , and David Sanders¹¹ 

¹ Department of Physics and Astronomy, University of California, Los Angeles, CA 90095-1547, USA; dxh@astro.ucla.edu

² School of Physics and Technology, Wuhan University, Wuhan 430072, People's Republic of China

³ Kavli Institute for the Physics and Mathematics of the Universe (WPI), The University of Tokyo, Kashiwa, Chiba 277-8583, Japan

⁴ Department of Astronomy, School of Science, The University of Tokyo, 7-3-1 Hongo, Bunkyo, Tokyo 113-0033, Japan

⁵ National Astronomical Observatory of Japan, Mitaka, Tokyo 181-8588, Japan

⁶ Korea Astronomy and Space Science Institute, Deajeon, 34055, Republic of Korea

⁷ Max-Planck-Institut für Astronomie, Königstuhl 17, D-69117, Heidelberg, Germany

⁸ Physics Department, California Polytechnic State University, San Luis Obispo, CA 93407, USA

⁹ School of Physics and Astronomy, Rochester Institute of Technology, 84 Lomb Memorial Drive, Rochester, NY 14623, USA

¹⁰ Space Telescope Science Institute, 3700 San Martin Drive, Baltimore, MD 21218, USA

¹¹ Institute for Astronomy, University of Hawaii, 2680 Woodlawn Drive, Honolulu, HI 96822, USA

Abstract

Correlations between the mass of a supermassive black hole (SMBH) and the properties of its host galaxy (e.g., total stellar mass M_* , luminosity L_{host}) suggest an evolutionary connection. A powerful test of a coevolution scenario is to measure the relations $\mathcal{M}_{\text{BH}}-L_{\text{host}}$ and $\mathcal{M}_{\text{BH}}-M_*$ at high redshift and compare with local estimates. For this purpose, we acquired *Hubble Space Telescope* (*HST*) imaging with WFC3 of 32 X-ray-selected broad-line (type 1) active galactic nuclei at $1.2 < z < 1.7$ in deep survey fields. By applying state-of-the-art tools to decompose the *HST* images including available ACS data, we measured the host galaxy luminosity and stellar mass along with other properties through the two-dimensional model fitting. The black hole mass (\mathcal{M}_{BH}) was determined using the broad $\text{H}\alpha$ line, detected in the near-infrared with the Subaru Fiber Multi-Object Spectrograph, which potentially minimizes systematic effects using other indicators. We find that the observed ratio of \mathcal{M}_{BH} to total M_* is $2.7\times$ larger at $z \sim 1.5$ than in the local universe, while the scatter is equivalent between the two epochs. A nonevolving mass ratio is consistent with the data at the 2σ – 3σ confidence level when accounting for selection effects (estimated using two independent and complementary methods) and their uncertainties. The relationship between \mathcal{M}_{BH} and host galaxy total luminosity paints a similar picture. Therefore, our results cannot distinguish whether SMBHs and their total host stellar mass and luminosity proceed in lockstep or whether the growth of the former somewhat overshoots the latter, given the uncertainties. Based on a statistical estimate of the bulge-to-total mass fraction, the ratio $\mathcal{M}_{\text{BH}}/M_{*,\text{bulge}}$ is offset from the local value by a factor of ~ 7 , which is significant even accounting for selection effects. Taken together, these observations are consistent with a scenario in which stellar mass is subsequently transferred from an angular momentum-supported component of the galaxy to a pressure-supported one through secular processes or minor mergers at a faster rate than mass accretion onto the SMBH.

Unified Astronomy Thesaurus concepts: [Galaxy evolution \(594\)](#); [Active galaxies \(17\)](#)

Supporting material: figure set

1. Introduction

Most galactic nuclei are thought to harbor a supermassive black hole (SMBH) whose mass (\mathcal{M}_{BH}) is known to correlate with the host properties, such as luminosity (L_{host}), stellar mass (M_*), and stellar velocity dispersion (σ_*). The tightness of these correlations (also known as scaling relations) may indicate a connection between nuclear activity and galaxy formation and evolution (e.g., Magorrian et al. 1998; Ferrarese & Merritt 2000; Gebhardt et al. 2001; Marconi & Hunt 2003; Häring & Rix 2004; Gültekin et al. 2009; Graham et al. 2011; Beifiori et al. 2012). Currently, the physical mechanism that can produce such a tight relationship is unknown due to the daunting range of scales between the dynamical sphere ($\sim \text{pc}$) of the SMBHs and their host galaxy ($\sim 10 \text{ kpc}$). On one hand, cosmological simulations of structure formation are able to reproduce the mean local correlations, possibly by invoking

active galactic nucleus (AGN) feedback as the physical connection (Springel et al. 2005; Di Matteo et al. 2008; Hopkins et al. 2008; DeGraf et al. 2015) or having them share a common gas supply (Cen 2015; Menci et al. 2016), not necessarily in a direct manner. On the other hand, there may not be a need for a physical coupling (Peng 2007; Hirschmann et al. 2010; Jahnke & Macciò 2011); the statistical convergence from galaxy assembly alone (i.e., mergers) may reproduce the observed correlations.

To understand the nature of these correlations, it is important to study them as a function of redshift, determining how and when they emerge and evolve over cosmic time (e.g., Treu et al. 2004; Salvander et al. 2006; Woo et al. 2006; Jahnke et al. 2009; Schramm & Silverman 2013; Sun et al. 2015). During the past decade, there has been much progress on this front using type 1 AGNs. For example, it has been demonstrated that AGN host galaxies, at $z < 1$ and for fixed

\mathcal{M}_{BH} , are underluminous compared to today’s hosts (Peng et al. 2006b; Treu et al. 2007; Park et al. 2015). Similarly, Woo et al. (2008) and Bennert et al. (2011b) found a positive evolution of \mathcal{M}_{BH} , especially when the data are sufficiently robust to isolate the luminosity or stellar mass of the bulge or spheroidal component. At $z > 1$, Merloni et al. (2010) decomposed the entire spectral energy distribution (SED) into a nuclear AGN and host galaxy components and found a positive evolution of the mass ratios of black holes to their host galaxies. However, the accuracy of such an approach for luminous AGNs has not yet been well established, as discussed herein. If realized, such offsets can be interpreted as a scenario in which SMBHs were built up first, then galaxies grew around their deep potential wells. A possible mechanism to account for the latter part of the growth of the galaxy without increasing \mathcal{M}_{BH} is the transfer of stellar mass from the disk to the bulge (Jahnke et al. 2009; Bennert et al. 2011a; Schramm & Silverman 2013) through bar instabilities or minor mergers.

However, there are studies (Cisternas et al. 2011; Schramm & Silverman 2013; Mechtley et al. 2016) based on *Hubble Space Telescope* (*HST*) imaging of deep survey fields such as COSMOS and CDFS that report no evolution in the $\mathcal{M}_{\text{BH}} - M_*$ mass ratio as compared to the local relation. In support, Sun et al. (2015) reanalyzed the mass ratios for broad-line AGNs in the COSMOS field in a similar manner (i.e., stellar mass measurements from SED fitting) to Merloni et al. (2010) and found no evolution when accounting for the selection effects described in Schulze & Wisotzki (2014), which consider the black hole mass function and Eddington rate distribution of the sample at their respective epochs.

To make substantial progress, it is important to construct statistical high- z samples that reduce the uncertainties, and carefully consider selection effects and inherent systematic errors. First, one needs to deal with the inherent uncertainties in black hole mass estimates using the so-called “virial” method. In particular, many studies rely on \mathcal{M}_{BH} estimates using the C_{IV} (or M_{gII}) line that may have unknown systematics, such as a nongravitational component of the gas dynamics of the broad-line region (BLR), when compared to local samples with masses based on broad Balmer lines (i.e., $H\alpha$ and $H\beta$; Baskin & Laor 2005; Trakhtenbrot & Netzer 2012; Schulze et al. 2018). Second, measurements of the host galaxy properties are challenging due to the overwhelming glare of the bright nuclear light. This ultimately requires careful modeling of the point-spread function (PSF) and, whenever possible, the use of lensed AGNs, since the magnification increases the spatial resolution (Peng et al. 2006b; Ding et al. 2017a, 2017b). Especially not to be overlooked, as in past studies, the selection function needs to be taken into account when interpreting the observations (Lauer et al. 2007; Treu et al. 2007). For instance, it was demonstrated by Schulze & Wisotzki (2011, 2014) that selecting bright AGNs at high redshift results in an $\mathcal{M}_{\text{BH}} - M_*$ relation with a steeper slope than if chosen randomly, suggesting that the selection effects are the culprit rather than an intrinsically faster or even existing evolution. It is also important to consider the selection function when comparing observed scaling relations with those from simulations (DeGraf et al. 2015).

In this study, we aim to make progress by utilizing a large sample with high-quality data for the measurement of both the \mathcal{M}_{BH} and the host properties, extending to higher redshifts where evolutionary effects should be strongest. In particular,

samples based on two-dimensional image analysis using *HST* at $z > 1$ are limited. To date, the infrared capabilities of *HST*/WFC3 have not been fully exploited on this topic. Here we measure the properties of 32 host galaxies with a redshift range of $1.2 < z < 1.7$ using *HST*/WFC3 imaging data and estimate their \mathcal{M}_{BH} based on the robust $H\alpha$ detections using the Subaru Fiber Multi-Object Spectrograph (FMOS). Given the high quality and sample size of our data, we are capable of testing whether the growth of a black hole predates that of the host by a factor of at least 1.7 (i.e., ~ 0.23 dex; Schulze & Wisotzki 2014). This value is the minimum offset expected for a nonevolving mass ratio as described in Section 2.3. Furthermore, we collect from the literature comparison samples of intermediate- z and local AGNs, selected to have been analyzed with very similar methods to those applied in the distant sample. We recalibrate the relevant quantities from the literature based on a set of self-consistent recipes to ensure that our differential measurement of evolution is robust to calibration and methodological issues (Section 2.4).

The paper is organized as follows. We describe the sample selection and black hole masses in Section 2. We describe the new *HST*/WFC3 observations, available *HST*/ACS imaging, and construction of a PSF library in Section 3. In Section 4, we describe our method to decompose the rest-frame optical emission and measure the host galaxy surface photometry. In Section 5, we use the multiband host magnitudes to infer the stellar population from which we apply to derive the rest-frame R -band L_{host} and M_* to compare with local relations. In addition, we use the information on the radial light distribution (i.e., Sérsic index) to infer the likely fraction of stars in the bulge ($M_{*,\text{bulge}}$) and its relation to the \mathcal{M}_{BH} . The discussion and conclusions are presented in Sections 6 and 7. Throughout this paper, we adopt a standard concordance cosmology with $H_0 = 70 \text{ km s}^{-1} \text{ Mpc}^{-1}$, $\Omega_m = 0.30$, and $\Omega_\Lambda = 0.70$. Magnitudes are given in the AB system. A Chabrier initial mass function (IMF) is employed consistently.

2. Experimental Design

We utilize a sample size of 32 broad-line (FWHM $> 2000 \text{ km s}^{-1}$; type 1) AGNs that have black hole mass measurements and fall within deep extragalactic survey fields that offer rich ancillary data. Specifically, we focus on meeting the following criteria to overcome the limitations of previous studies.

1. Black hole mass estimates (\mathcal{M}_{BH}) are based on Balmer lines (i.e., $H\alpha$), which avoid potential systematic uncertainties in UV-based estimators (Greene & Ho 2005).
2. Black holes masses $\mathcal{M}_{\text{BH}}/M_\odot \lesssim 8.7$ are below the knee of the black hole mass function to minimize selection biases (see Figure 1, top panel).
3. Eddington ratios are above 5% to further ensure homogeneity.
4. The X-ray-selected sample has host-to-total flux ratios typically above 30%, which facilitates the galaxy mass measurements.
5. The *HST*/WFC3 imaging of the host galaxy at a rest-frame wavelength of $\sim 5500 \text{ \AA}$, which is above the 4000 \AA break and does not include the broad $H\alpha$ line (6563 \AA), ensures sensitivity to the total stellar mass

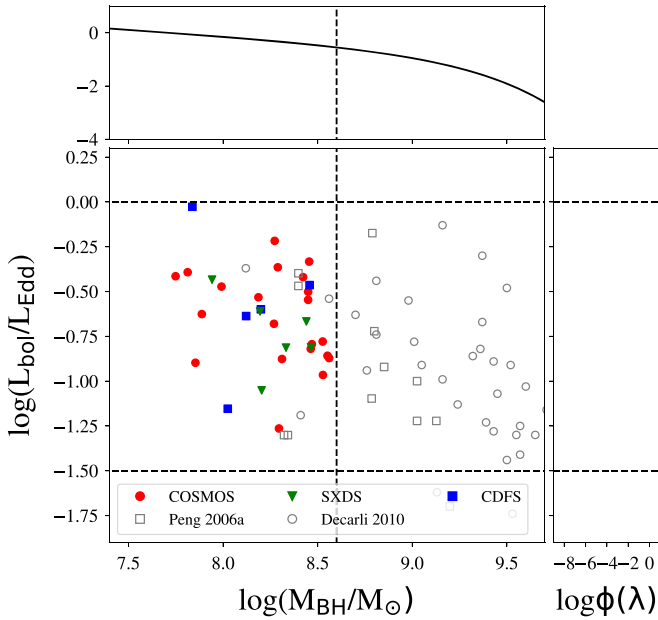


Figure 1. Selection window used to choose our AGN sample based on \mathcal{M}_{BH} and Eddington ratios ($\lambda = L_{\text{bol}}/L_{\text{Edd}}$). As indicated by the vertical dashed line, our sample (color-coded) falls below the knee of the black hole mass function at $z = 1.5$ (top panel; Schulze et al. 2015). On the right, we illustrate the shape of the Eddington rate distribution at these redshifts from the same reference. For comparison, we plot the high- z luminous SDSS AGN samples that have been studied with *HST* (gray squares and circles from Peng et al. 2006a and Decarli et al. 2010, respectively) mainly at the high-mass end.

content. This is somewhat coupled to the previous item in this list.

6. A large fraction of the sample has additional *HST* imaging (i.e., ACS), providing color information to achieve reliable K-corrections and stellar mass determinations.

2.1. Sample Selection

The 32 AGNs were initially selected by the X-ray observations of COSMOS (Civano et al. 2016), (E)-CDFs-S (Lehmer et al. 2005; Xue et al. 2011), and SXDS (Ueda et al. 2008) fields. In most cases, the X-ray sources are first identified as broad-line AGNs through optical spectroscopic campaigns with the Very Large Telescope, Keck, and *Magellan*. Follow-up near-infrared spectroscopic observations of the AGNs in these fields are carried out with Subaru’s FMOS (Kimura et al. 2010; Nobuta et al. 2012; Matsuoka et al. 2013), covering the wavelength range 0.9–1.8 μm , which provides the favorable $\text{H}\alpha$ and $\text{H}\beta$ lines out to $z \sim 1.7$ to estimate the \mathcal{M}_{BH} . Recently, Schulze et al. (2018) presented near-IR spectroscopy of a large compilation of 243 X-ray AGNs in these fields. It is from this catalog that we primarily select our targets. The continuum fitting and emission-line modeling provided by this work are performed through a common procedure for spectral model fits. This approach first corrects the spectra for galactic extinction and shifts them to the rest frame. The spectral regions in the near-IR that are strongly affected by OH emission are masked. The spectrum is modeled by both a narrow-line and a broad-line AGN template, and the emission-line information is inferred based on χ^2 minimization. We refer the reader to the aforementioned paper for further details. Note that three CDFS objects (i.e., CDFS-1, CDFS-229, and CDFS-724) are not included in Schulze et al. (2018); their infrared spectra are provided by Suh et al. (2015) using a similar approach.

Based on the \mathcal{M}_{BH} estimates described below (Section 2.2), we select targets with masses in the range $7.5 \lesssim \log(\mathcal{M}_{\text{BH}}/M_{\odot}) \lesssim 8.5$. The bolometric luminosities are measured from the broad AGN lines by Schulze et al. (2018; Section 3.3), which are used to calculate their Eddington ratio $\lambda = L_{\text{bol}}/L_{\text{Edd}}$. The flux-limited nature of the sample results in a slightly higher Eddington ratio distribution at lower \mathcal{M}_{BH} , as shown in Figure 1. Moreover, we have a higher preference to select targets that have rest-frame UV images (i.e., *HST*/ACS), as provided by Scoville et al. (2007) and Koekemoer et al. (2007) in the COSMOS field. We list the 32 AGNs observed with *HST*/WFC3 and analyzed in this work in Table 1, sorted by field and redshift.

2.2. Details of Black Hole Mass Estimates

The \mathcal{M}_{BH} of type 1 AGNs can be determined using the so-called virial method (Peterson et al. 2004; Shen 2013). The kinematics of the BLR trace the gravitational field of the central SMBH, assuming the gravity dominates the motion of the BLR gas. Under these assumptions, the width of the emission line provides the scale of the velocity dispersion (ΔV), while the AGN continuum luminosity establishes an empirical scale of the BLR size (R_{BLR}). The estimation of \mathcal{M}_{BH} is then achieved using these measurements, i.e., $\mathcal{M}_{\text{BH}} \simeq G^{-1} R_{\text{BLR}} \Delta V^2$ (McLure & Dunlop 2004).

To avoid any systematic bias between samples in the literature, we adopt a class of self-consistent estimators for our analysis. We first compare the estimators implemented in Schulze et al. (2018) and Ding et al. (2017b) and find very consistent $\text{H}\beta(\text{FWHM}(5100))$ -based masses (\mathcal{M}_{BH} rms < 0.03 dex). However, there is an ~ 0.2 dex inconsistency in their $\text{H}\alpha$ mass estimates. Therefore, we utilize the AGNs in Schulze et al. (2018) that have both $\text{H}\alpha$ and $\text{H}\beta$ lines (35 AGNs in total) and carry out a cross-calibration to determine which $\text{H}\alpha$ estimator has the best agreement between the two lines. As a result, the $\text{H}\alpha$ estimator in Schulze et al. (2018) has better agreement with $\text{H}\beta$. Thus, we adopt the scheme given in Schulze et al. (2018) for all AGN samples used in this study, including the comparison samples described below:

$$\log\left(\frac{\mathcal{M}_{\text{BH}}(\text{H}\alpha)}{M_{\odot}}\right) = 6.71 + 0.48 \log\left(\frac{L_{\text{H}\alpha}}{10^{42} \text{erg s}^{-1}}\right) + 2.12 \log\left(\frac{\text{FWHM}(\text{H}\alpha)}{1000 \text{ km s}^{-1}}\right) \quad (1)$$

and

$$\log\left(\frac{\mathcal{M}_{\text{BH}}(\text{H}\beta)}{M_{\odot}}\right) = 6.91 + 0.50 \log\left(\frac{L_{\lambda 5100}}{10^{44} \text{erg s}^{-1}}\right) + 2.0 \log\left(\frac{\text{FWHM}(\text{H}\beta)}{1000 \text{ km s}^{-1}}\right). \quad (2)$$

Note that these recipes are first provided by Vestergaard & Peterson (2006). Using these recipes, we estimate \mathcal{M}_{BH} by adopting the emission-line properties as measured by Schulze et al. (2018) for all 32 AGNs. While 14 AGNs have emission-line properties for both $\text{H}\alpha$ and $\text{H}\beta$, we adopt the value of \mathcal{M}_{BH} based on the $\text{H}\alpha$ emission line to have consistency across the sample. While most recipes are calibrated against $\text{H}\beta$, the line is typically weaker than $\text{H}\alpha$, hence lower signal-to-noise. We provide the \mathcal{M}_{BH} measurements, together with the properties of the emission lines, in Table 2.

Table 1
Details of Observation

Object ID (1)	z (2)	WFC3/Filter (3)	R.A. (4)	Decl. (5)	Observing Date (6)
COSMOS-CID 1174	1.552	F140W	150.2789	1.9595	2017 Oct 26
COSMOS-CID 1281	1.445	F140W	150.4160	2.5258	2018 Nov 26
COSMOS-CID 206	1.483	F140W	149.8371	2.0088	2017 Oct 23
COSMOS-CID 216	1.567	F140W	149.7918	1.8729	2017 Oct 23
COSMOS-CID 237	1.618	F140W	149.9916	1.7243	2018 Jun 3
COSMOS-CID 255 ¹²	1.664	F140W	150.1017	1.8483	2019 Mar 16
COSMOS-CID 3242	1.532	F140W	149.7113	2.1452	2017 Oct 26
COSMOS-CID 3570	1.244	F125W	149.6411	2.1076	2017 Oct 27
COSMOS-CID 452	1.407	F125W	150.0045	2.2371	2017 Oct 25
COSMOS-CID454	1.478	F140W	149.8681	2.3307	2018 Feb 26
COSMOS-CID 50	1.239	F125W	150.2080	2.0833	2017 Oct 23
COSMOS-CID 543	1.301	F125W	150.4519	2.1448	2018 Apr 30
COSMOS-CID 597	1.272	F125W	150.5262	2.2449	2018 Nov 25
COSMOS-CID 607	1.294	F125W	150.6097	2.3231	2017 Oct 25
COSMOS-CID 70	1.667	F140W	150.4051	2.2701	2017 Oct 27
COSMOS-LID 1273	1.617	F140W	150.0565	1.6275	2017 Oct 31
COSMOS-LID 1538	1.527	F140W	150.6215	2.1588	2018 May 1
COSMOS-LID 360	1.579	F140W	150.1251	2.8617	2017 Oct 30
COSMOS-XID 2138	1.551	F140W	149.7036	2.5781	2017 Nov 1
COSMOS-XID 2202	1.516	F140W	150.6530	1.9969	2017 Nov 5
COSMOS-XID 2396	1.600	F140W	149.4779	2.6425	2017 Nov 12
CDFS-1	1.630	F140W	52.8990	-27.8600	2018 Apr 3
CDFS-229	1.326	F125W	53.0680	-27.6580	2018 Apr 4
CDFS-321	1.570	F140W	53.0486	-27.6239	2018 Aug 18
CDFS-724	1.337	F125W	53.2870	-27.6940	2018 Apr 5
ECDFS-358	1.626	F140W	53.0850	-28.0370	2018 Feb 9
SXDS-X1136	1.325	F125W	34.8925	-5.1498	2018 Jan 29
SXDS-X50	1.411	F125W	34.0267	-5.0602	2018 Mar 1
SXDS-X717	1.276	F125W	34.5400	-5.0334	2018 Jul 2
SXDS-X735	1.447	F140W	34.5581	-4.8781	2017 Nov 14
SXDS-X763	1.412	F125W	34.5849	-4.7864	2018 Jul 3
SXDS-X969	1.585	F140W	34.7594	-5.4291	2018 Jul 2

Note. Column 1: object field and ID. Column 2: spectroscopic redshift. Column 3: WFC3 filter. Note that the targets from the COSMOS field also have ACS imaging. Columns 4 and 5: J2000 R.A. and decl. coordinates. Column 6: observing start date. The total exposure time of each target is 2394 s.

It is worth noting that the absolute flux calibration of the FMOS spectra is set to match the available ground-based IR imaging, UltraVISTA in the case of COSMOS. While an initial flux calibration is performed during the reduction of the FMOS data using calibration stars, there can be differential flux loss due to aperture effects, variable seeing conditions, and minor alignment issues with the instrument. The flux normalization is effectively an aperture correction in the J or H band, depending on the source redshift. We note that this procedure does not correct for intrinsic variability that may induce an additional error of 0.2 mag. We refer the reader to Section 2.2 of Schulze et al. (2018) for full details of the flux calibration.

2.3. Expected Bias from the Selection Function

Our AGN sample is primarily selected based on the value of \mathcal{M}_{BH} and the Eddington ratio. It is well known that sample selection effects must be taken into account in order to interpret the observed black hole–host relations and measure their evolution with redshift, thus avoiding biases (Treu et al. 2007; Bennert et al. 2011a; Schulze & Wisotzki 2011, 2014; Park et al. 2015). The main source of bias is due to the fact that active samples are necessarily selected based on properties that correlate with black hole mass estimators (such as AGN

luminosity, line strength, and width), and thus one tends to favor overly massive black holes in the presence of intrinsic scatter and observational errors. Correcting for observational biases requires a well-characterized selection function, such as the one we have for our sample; a model of the black hole mass function; and the evolution of the correlations between \mathcal{M}_{BH} and other properties.

Given our selection function, we use the Bayesian framework introduced by Schulze & Wisotzki (2011, 2014) to estimate the expected bias. In this framework, under the assumption of no evolution of the correlations between \mathcal{M}_{BH} and host galaxy properties, one can compute the expected bias for a given sample prior to the observations. The key ingredients of this model are the local \mathcal{M}_{BH} host galaxy property correlations, black hole mass function, and Eddington ratio distribution at the redshift of observation. The latter two quantities are estimated from the type 1 AGN distributions (Schulze et al. 2015) and corrected to represent the parent population of all active SMBH hosts.

Adopting our specific selection limits into the framework (i.e., $\log(\mathcal{M}_{\text{BH}}/M_{\odot}) \in [7.5, 8.56]$, $\log(L_{\text{bol}}/L_{\odot}) \in [45.0, 46.2]$, and $\log(\lambda) \in [-2.0, 0.5]$), we infer an expected bias of +0.21 dex in the observed $\Delta \log(\mathcal{M}_{\text{BH}})$ for samples at $z \sim 1.5$, assuming the baseline choices for the inputs to the model that include the local

Table 2
AGN Properties

Target ID	H α Emission Line				H β Emission Line			
	FWHM(H α) (km s $^{-1}$)	log($L_{\text{H}\alpha}$) (erg s $^{-1}$)	log \mathcal{M}_{BH} (M_{\odot})	Eddington Ratio (log($L_{\text{Bol}}/L_{\text{Edd}}$))	FWHM(H β) (km s $^{-1}$)	log($L_{\lambda 5100}$) (erg s $^{-1}$)	log \mathcal{M}_{BH} (M_{\odot})	Eddington Ratio (log($L_{\text{Bol}}/L_{\text{Edd}}$))
(1)	(2)	(3)	(4)	(5)	(6)	(7)	(8)	(9)
CID 1174	1906	43.43	7.99	-0.47	5898	44.76	8.83	-1.34
CID 1281	1619	43.24	7.75	-0.41
CID 206	3334	43.48	8.53	-0.97
CID 216	2230	42.85	7.85	-0.90
CID 237	2112	43.86	8.29	-0.36
CID 255	1932	43.99	8.27	-0.22	3709	45.37	8.73	-0.60
CID 3242	2543	43.83	8.45	-0.55	3775	45.10	8.61	-0.75
CID 3570	1959	43.16	7.89	-0.63
CID 452	3458	42.92	8.30	-1.26	3127	44.63	8.22	-0.88
CID 454	2824	43.34	8.31	-0.88
CID 50	2340	43.94	8.42	-0.42	1939	45.33	8.15	-0.06
CID 543	2189	43.57	8.19	-0.53
CID 597	1656	43.33	7.81	-0.39
CID 607	3009	43.67	8.53	-0.78	4242	44.78	8.56	-1.04
CID 70	2480	43.51	8.27	-0.68	3982	45.16	8.69	-0.77
LID 1273	3224	43.61	8.56	-0.87
LID 1538	2941	43.60	8.47	-0.79
LID 360	2482	43.88	8.45	-0.50	2869	45.09	8.37	-0.52
XID 2138	3186	43.61	8.55	-0.86	2945	44.81	8.25	-0.71
XID 2202	2973	43.56	8.46	-0.82
XID 2396	2271	44.06	8.46	-0.33	2658	45.50	8.51	-0.24
CDFS-1	2000	43.02	7.83	-0.03
CDFS-229	2190	43.60	8.20	-0.60
CDFS-321	2442	43.93	8.46	-0.46
CDFS-724	2541	42.95	8.03	-1.15
ECDIFS-358	2237	43.40	8.12	-0.64
SXDS-X1136	2760	43.43	8.33	-0.81	6761	44.71	8.93	-1.49
SXDS-X50	1817	43.42	7.94	-0.43
SXDS-X717	2931	43.05	8.20	-1.05
SXDS-X735	2702	43.70	8.44	-0.67	3520	45.07	8.54	-0.70
SXDS-X763	2961	43.57	8.47	-0.81	4509	44.51	8.47	-1.29
SXDS-X969	2296	43.50	8.20	-0.61	1696	45.05	7.90	-0.08

Note. Column 1: object ID. Columns 2–5: H α emission-line width (FWHM), H α luminosity, inferred \mathcal{M}_{BH} , and Eddington ratio. Columns 6–9: H β emission-line black hole properties. The typical uncertainty level for FWHM is 15%, and for log(L_{λ}), it is in the range 0.01 \sim 0.2 dex, respectively. The inferred uncertainty level for \mathcal{M}_{BH} is assumed as 0.4 dex.

value of the mass $\mathcal{M}_{\text{BH}}/M_{*}$ ratio. To reiterate, an offset in the observed mass relations of 0.2 dex at $z \sim 1.5$ can be considered consistent with no evolution in the mass ratio. This bias correction should be considered an approximate estimate, with an uncertainty that depends on the uncertainty of the inputs. Furthermore, if the scaling relations actually evolve, one needs to introduce a model for the evolution in order to infer the underlying bias-corrected trends. We will revisit these issues in Section 5.5.

2.4. Comparison Samples

We make use of the $\mathcal{M}_{\text{BH}}-L_{\text{host}}$ and $\mathcal{M}_{\text{BH}}-M_{*}$ relations in the literature for comparison with our high- z data. For the local relation, we use the measurements of Bennert et al. (2010) and Bennert et al. (2011a, hereafter B10 and B11) to define our zero-point for local AGN samples. The sample by B10 consists of 19 AGNs with the $\mathcal{M}_{\text{BH}}-L_{\text{host}}$ relation determined with reliable \mathcal{M}_{BH} masses using reverberation mapping with an uncertainty level of ~ 0.15 dex. Note that B10 only provided the single-galaxy V -band luminosity. Ding et al. (2017b) derived the galaxy R -band luminosity based on the same early-type galaxy template spectrum adopted by B10 using

K-correction (see Section 3.2 therein). The work of B11 contains 25 local active AGNs, where the \mathcal{M}_{BH} are measured using the single-epoch method (\mathcal{M}_{BH} uncertainty level ~ 0.4 dex). To track the local M_{*} and \mathcal{M}_{BH} relations to higher values, we include 30 inactive galaxies (mainly ellipticals or S0) from Häring & Rix (2004, hereafter HR04). It is worth noting that the local inactive sample is mainly bulge-dominated, and we adopt the bulge mass for the entire local sample. In other words, our local comparison is the $\mathcal{M}_{\text{BH}}-M_{*,\text{bulge}}$ and not those involving total quantities.

We include in our analysis published samples at intermediate redshifts to understand the evolution of these correlations. We select samples that were analyzed by members of our team to ensure uniform measurements. The intermediate-redshift AGNs that we include are 52 objects published by Park et al. (2015) using a single band that are applicable for the $\mathcal{M}_{\text{BH}}-L_{\text{host}}$ relation at $0.36 < z < 0.57$ and 27 objects published by Bennert et al. (2011b) and Schramm & Silverman (2013) at $0.5 < z < 1.9$. Similar to the B10 sample, the R -band luminosities of these intermediate-redshift systems (79 in total) are obtained by Ding et al. (2017b) using K-corrections from the V band based on the same stellar template. Moreover,

Bennert et al. (2011b) and Schramm & Silverman (2013) estimated the stellar masses of their 27 objects using multiband imaging data, and we adopt them as the $\mathcal{M}_{\text{BH}}-M_*$ comparison sample. In addition, we adopt a sample of 32 $\mathcal{M}_{\text{BH}}-M_*$ measurements at $0.3 < z < 0.9$ by Cisternas et al. (2011) to compare with our sample. Across the intermediate-redshift sample, we recalibrate the \mathcal{M}_{BH} using the self-consistent recipes introduced in Section 2.2 including those estimated from Mg_{II} using the recipe in Ding et al. (2017b).

The values for all of the $\mathcal{M}_{\text{BH}}-L_{\text{host}}$ comparison samples are listed in Ding et al. (2017b; Tables 1 and 2 therein). The $\mathcal{M}_{\text{BH}}-M_*$ comparison samples are collected and summarized here in Appendix B, Table 7.

3. HST Observations

High spatial resolution imaging is required for the decomposition of the nuclear and host emission to accurately estimate the luminosity and stellar mass of the host galaxy. For this purpose, we observed the sample of 32 AGNs, as described above, with the *HST*/WFC3 infrared channel through *HST* program GO-15115 (PI: John Silverman). We selected the filters F125W ($1.2 < z < 1.44$) and F140W ($1.44 < z < 1.7$) according to the redshift of the targets so that the rest-frame spectral window is well above the 4000 Å break. This selection further ensures that the broad $\text{H}\alpha$ line is not present in the bandpass so as not to contaminate the host emissions due to the broad wings of the PSF.

For each target, we obtained six separate exposures of 399 s (i.e., total exposure time 2394 s). The six exposures were dithered and combined with the ASTRODRIZZLE software package following standard procedures and resulted in an output pixel scale of $0''.0642$ by setting the `pixfrac` parameter as 0.8 and using a Gaussian kernel.¹² In Table 1, we list the details of the individual observations.

Having obtained the *HST* image, we remove the background light arising from the sky and the detector. In this step, we adopt PHOTUTILS by Python and model the global background light in two dimensions based on the SExtractor algorithm, which effectively accounts for gradient in the background distribution. Then, we subtract the derived sky background light to obtain a clear image. To test the fidelity of this subtraction, we measure the surface brightness in the empty regions and verify that it is consistent with zero within the noise. Finally, we extract the postage stamp of the AGN and PSF images to carry out the modeling process; see Sections 3.1 and 4.

Multiband information provides the SED at a more precise level. A substantial fraction (21/32) of our objects have rest-frame UV images for those in COSMOS (Koekemoer et al. 2007). Here we utilize images taken with the ACS/F814W filter. The final image is drizzled to $0''.03$ pixel scale. Given the multiband images for our AGNs, we are able to infer their host color and assess the contribution of both the young and old stellar population, which ensures an accurate inference of rest-frame *R*-band luminosity (including a *K*-correction) and stellar mass (Gallazzi & Bell 2009).

The knowledge of the PSF is crucial for imaging the decomposition of the AGN and its host, especially when the point source contributes to the majority of the total emission. The PSF is known to vary across the detector and over time due to the effects of aberration and breathing. Simulated PSFs, such as those based on TINYTIM, are usually insufficient for our purposes (Mechtley et al. 2012). Stars within the field of view of each observation provide a better description than the simulated PSF, since they are observed simultaneously with the science targets and reduced and analyzed in a consistent manner (Kim et al. 2008; Park et al. 2015). However, we have found that such stars usually do not provide an ideal PSF for deblending the AGN and host galaxy through extensive tests. The issues are associated with an insufficient number of bright stars near our targets, color differences, and other effects not fully understood.

To minimize the impact of such mismatches, we build a PSF library by selecting all of the isolated, unsaturated PSF stars with high signal-to-noise ratio from our entire program. The selection consists of the following steps. First, we identify stars from the COSMOS2015 catalog (Laigle et al. 2016). However, many bright stars with an intensity similar to our AGN sample were excluded in this catalog. Therefore, we also manually select PSF-like objects as candidates from the *HST*/WFC3 imaging. We then discard nonideal PSF candidates based on their intensity, FWHM, central symmetry, and presence of nearby contaminants. In total, the PSF library contains 78 and 37 stars imaged through filters F140W and F125W, respectively. We assume that the stars in the library are representative of the possible PSFs in our program. The dispersion of PSF shapes within our library provides us with a good representation of the level of uncertainty in our measurements resulting from the image decomposition.

4. AGN–Host Decomposition

We simultaneously fit the two-dimensional flux distribution of the central AGN and the underlying host galaxy. Following common practice, we model the central AGN as a scaled point source and the host galaxy as a Sérsic profile. Note that the actual morphologies of the host galaxies could be more complicated (e.g., bulge+disk). However, the Sérsic model is an adequate first-order approximation of the surface brightness distribution with a flexible parameterization that provides sufficient freedom to infer the total host flux, even for our high-redshift sample. We simultaneously fit the nearby galaxies that happen to be close enough to the AGN with a Sérsic model to account for any potential contamination from their extended profiles. The systems CID 206 and ECDFS-358 have nearby objects that could not be described by the Sérsic model; thus, we mask these objects in the fitting procedure.

We use the image modeling tool LENSTRONOMY (Birrer et al. 2015; Birrer & Amara 2018) to perform the decomposition of the host and nuclear light. LENSTRONOMY is a multipurpose, open-source, gravitational lens image forward-modeling package written in Python. Its flexibility enables us to turn off the lensing channel and focus on the AGN and host decomposition.¹³ The main advantage of LENSTRONOMY is

¹² For CID 255, 3/6 of the dither WFC3 images are corrupted. We analyze this sample using the same approach, taking the three available frames.

¹³ As a check, we compared the results from LENSTRONOMY to the commonly used galaxy modeling software GALFIT and confirmed that the results are consistent between the two.

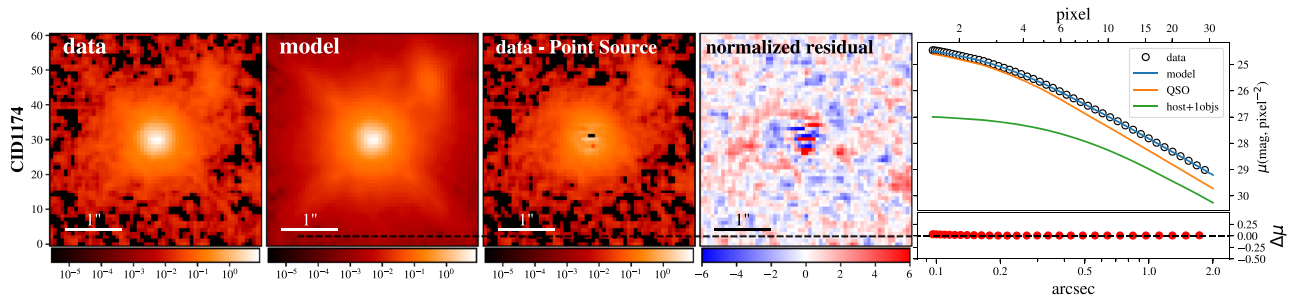


Figure 2. The AGN–host galaxy decomposition of COSMOS-CID 1174 based on the *HST*/WFC3 F140W image. The panels from left to right are as follows: (1) observed data, (2) best-fit model (AGN+host), (3) data minus the model PSF (i.e., host galaxy free of the AGN), (4) residuals divided by the variance, and (5) one-dimensional surface brightness profiles (top) and the corresponding residual (bottom). The one-dimensional profiles indicate the surface brightness, including the data (open circles), best-fit model (blue line), AGN (orange line), and model for the extended sources (green line; i.e., host and other objects). Note that the one-dimensional surface brightness profiles are only for illustration purposes. The actual fitting is based on the two-dimensional images.

(The complete figure set (32 images) is available.)

that it returns the full posterior distribution of each parameter (i.e., not just the best-fit model) and the Laplace approximation of the uncertainties. The input ingredients for LENSTRONOMY include the following.

1. AGN imaging data. Using aperture photometry, we find that an aperture size with radius $\sim 1''.5$ sufficiently covers the AGN emission of our sample.¹⁴ By default, we extract an image of 61×61 pixels (i.e., $4'' \times 4''$). If needed, a larger box size is selected to include nearby objects.
2. Noise level map. The origin of the noise in each pixel stems from the read, background, and Poisson noise from the astronomical sources themselves. We measure these directly from the empty regions of the data. We then calculate the effective exposure time of each pixel based on the drizzled WHT array maps to infer the Poisson noise level. A final noise map includes all of these sources of error.
3. PSF. The PSF is taken directly from the PSF library. Usually, a mismatch exists when subtracting the AGN as the scaled PSF, especially at the central parts. While modeling multiply imaged AGNs, this mismatch can be mitigated with PSF reconstruction by the iterative method (Chen et al. 2016; Birrer et al. 2019). However, this approach requires multiple images that are not available in our case. We remedy this deficiency by using a broad library that should contain sufficient information to cover all possible PSFs.

The host property of an AGN is determined by the following steps. First, we model the AGN and host using each PSF in the library. With the input ingredients to LENSTRONOMY, the posterior distribution of the parameter space is calculated and optimized by adopting the Particle Swarm Optimizer (PSO¹⁵; Kennedy & Eberhart 1995). To avoid any unphysical results,

¹⁴ The photometric aperture was determined as a compromise between the detection of the total flux and a minimization of the background noise while keeping the computational time low. We found that extending the radius beyond $1''.5$ did not add any missing light, while it increased the noise and computational time.

¹⁵ Note that LENSTRONOMY enables one to further infer the parametric confidence interval using Markov Chain Monte Carlo. In our case, given a fixed PSF, the 1σ inference of each parameter is extremely narrow. Thus, we only take the best-fit inference using PSO for further calculations. The errors on the fit parameters are assessed by using different PSFs for each object in the sample.

we set the upper and lower limits on the parameters: effective radius $R_{\text{eff}} \in [0''.1, 1''.0]$, Sérsic index $n \in [0.3, 7]$. Then, we rank the performance of each PSF based on the χ^2 value and select the top eight PSFs as representative of the best-fit PSFs. We determine the host Sérsic parameters (i.e., flux, R_{eff} , Sérsic index) using a weighted arithmetic mean, calculated as follows:

$$w_i = \exp\left(-\alpha \frac{(\chi_i^2 - \chi_{\text{best}}^2)}{2\chi_{\text{best}}^2}\right), \quad (3)$$

where α is an inflation parameter¹⁶ so that when $i = 8$,

$$\alpha \frac{\chi_{i=8}^2 - \chi_{\text{best}}^2}{2\chi_{\text{best}}^2} = 2. \quad (4)$$

The goal of this recipe is to weight each PSF based on its relative goodness of fit while ensuring that at least eight are used to capture the range of systematic uncertainties. The results do not change significantly if we chose a different number of PSFs, as shown below.

Note that since each AGN was observed at a different location of the detector and at a different time, the top eight PSFs usually vary from one AGN to another. Given the weights, the values of the host properties and the rms (σ) error are calculated as

$$\bar{x} = \frac{\sum_{i=1}^N x_i * w_i}{\sum w_i}, \quad (5)$$

$$\sigma = \sqrt{\frac{\sum_{i=1}^N (x_i - \bar{x})^2 * w_i}{\sum w_i}}, \quad (6)$$

where N is the number of the ranking PSF, i.e., $N = 8$. In Figure 2, we demonstrate the best-fit result for COSMOS-CID 1174. The adopted weights are listed in Table 3.

We apply this approach to all AGNs to determine the global characteristics of the hosts of type 1 AGNs at these high redshifts. We measure the effective radius (R_{eff}), Sérsic index, and host-to-total flux ratio and describe each of these in the following section. We recognize that these measurements are weighted by the eight top-ranked PSFs. The limited number of

¹⁶ Defining α as the inflation parameter literally means that it has to be larger than 1. If $\alpha < 1$, the relative likelihood between different PSFs would be too close, and introducing α would have a side effect.

Table 3
Host Galaxy Measurements of CID 1174

PSF Rank (1)	Total χ^2 (2)	Weights w_i (3)	Host Flux (counts) (4)	Host Flux Ratio (5)	R_{eff} (arcsec) (6)	Sérsic n (7)
1	8584.429	1.000	82.2	35%	0".345	1.1
2	8646.711	0.920	99.1	42%	0".298	1.9
3	8816.947	0.734	76.7	33%	0".365	1.1
4	9304.841	0.383	128.6	55%	0".231	2.8
5	9652.575	0.241	187.5	79%	0".116	6.2
6	9917.101	0.170	100.2	42%	0".287	2.1
7	10018.324	0.148	75.1	32%	0".365	1.2
8	10087.456	0.135	79.8	34%	0".358	1.2
Weighted value			97.322 \pm 28.336	42% \pm 12%	0".309 \pm 0".065	1.9 \pm 1.3

Note. Column 1: rank of the PSF from the library. Column 2: total χ^2 for the corresponding PSF. Column 3: weights for the inference. Columns 4–7: fitted value for the host flux, host/total flux ratio, effective radius, and Sérsic index. For this sample, the inflation parameter α calculated by Equation (4) is 16.671.

top-ranked PSFs may underestimate actual uncertainties. To gauge how the number of top-ranked PSFs affects our results, we compare results when also using five and 10 top-ranked PSFs. As shown in Figure 3, the results are consistent. For each AGN, we check the location on the detector for the top-ranked PSFs and find that they are unrelated to the AGN position on the detector. This finding underscores that position on the detector is not the main factor driving the PSF shape. Other factors, likely to be more significant, are the subpixel centering, the intrinsic color of the star, and the jitter and thermal status of the telescope during the observations. The complexity of the problem highlights the necessity of decomposing the AGN using all available PSF stars from the entire program.

We carry out a similar analysis for 21/32 AGNs in the COSMOS field that have ACS/F184W imaging data. We assess their host flux ratio using the same approach as for the WFC3-IR. The ACS field of view is more extensive than the WFC3 one; thus, we generated 174 PSFs for use. As expected, the detection of the host galaxy in the IR band is of higher significance than the UV due to the effects of dust extinction and the contrast between the (blue) AGN and (red) host. Thus, we fix the R_{eff} and Sérsic n as the value determined by the IR band, thus amounting to an assumption that the morphology of the galaxy is consistent between the ACS and WFC3 bands. In this case, the only free parameters are the total host and AGN flux. We report the host galaxy properties in Table 4.

5. Results

From our image decomposition, we detect the host galaxy in all cases at a significant level, except one case (i.e., SXDS-X763) that has a host-to-total flux ratio lower than 15%. The *HST*/WFC3 images with the AGN component removed are presented in the third panel (i.e., the “data point source” stamps) of Figure 2 and its Figure Set for the remaining cases. While some of the galaxies have nearby neighbors, most are isolated and do not show strong signs of interaction or ongoing mergers, which indicates that the fueling mechanism of AGNs may not be from major mergers for our sample. This is also relevant for model fitting with smooth Sérsic profiles and the subsequent determination of the stellar mass. In the following subsections, we describe the properties of our ensemble of type 1 AGN host galaxies.

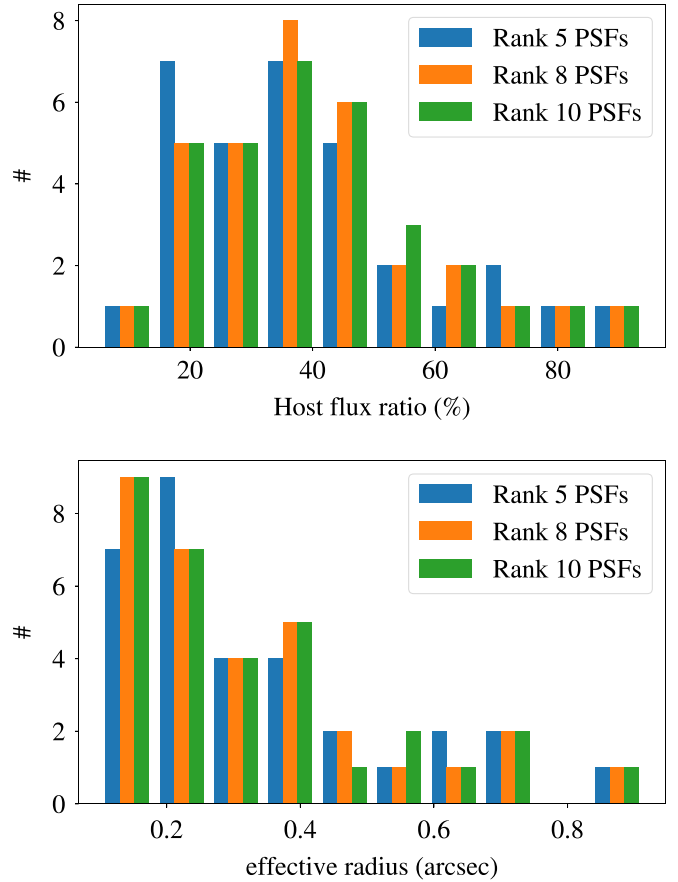


Figure 3. Distribution of the host-to-total flux ratio and effective radius when implementing a different number of top-ranked PSFs.

5.1. Host Galaxy Properties

As shown in Figure 3 (top panel), the host-to-total flux ratio (total = host+nuclear) of the sample spans a wide range, from 10% to 90%, with most of the sample concentrated between 20% and 50% (median value 37%). Those with flux ratios above \sim 20% have a higher degree of significance with respect to the detection of the host galaxy, while the five systems (i.e., CID 255, CID 50, LID 360, CDFS-229, SXDS-X763) that have host-to-total flux ratios lower than 20% should be considered as marginal detections.

Table 4
Host Galaxy Properties

Target ID	WFC3					ACS/F814W			Derived Properties		
	χ^2 (Reduced)	Host–Total Flux Ratio	R_{eff} (arcsec)	Sérsic n	Magnitude (AB system)	χ^2 (Reduced)	Host–Total Flux Ratio	Magnitude (AB system)	$\log L_R$ ($L_{\odot,R}$)	$\log M_*$ (M_{\odot})	$\log M_{*,\text{Bulge}}$ (M_{\odot})
(1)	(2)	(3)	(4)	(5)	(6)	(7)	(8)	(9)	(10)	(11)	(12)
CID 1174	2.307	42% ± 12%	0".31 ± 0".07	1.9 ± 1.3	21.48 ^{+0.37} _{-0.28}	2.496	11% ± 1%	23.21 ^{+0.11} _{-0.11}	11.01 ^{+0.15} _{-0.15}	10.63 ^{+0.18} _{-0.18}	10.21 ^{+0.40} _{-0.53}
CID 1281	1.322	49% ± 14%	0".24 ± 0".09	3.2 ± 1.5	22.88 ^{+0.36} _{-0.27}	1.378	19% ± 8%	24.83 ^{+0.60} _{-0.38}	10.38 ^{+0.15} _{-0.15}	10.00 ^{+0.18} _{-0.18}	9.77 ^{+0.28} _{-0.51}
CID 206	2.054	35% ± 24%	0".29 ± 0".15	3.1 ± 2.5	21.82 ^{+1.30} _{-0.58}	1.903	8% ± 2%	23.67 ^{+0.40} _{-0.29}	10.83 ^{+0.52} _{-0.23}	10.45 ^{+0.53} _{-0.25}	10.14 ^{+0.52} _{-0.62}
CID 216	1.514	94% ± 5%	0".25 ± 0".06	6.2 ± 1.2	21.51 ^{+0.05} _{-0.05}	1.425	35% ± 2%	23.45 ^{+0.05} _{-0.05}	11.01 ^{+0.03} _{-0.03}	10.63 ^{+0.10} _{-0.10}	10.52 ^{+0.15} _{-0.25}
CID 237	2.349	30% ± 6%	0".87 ± 0".17	4.7 ± 1.7	21.28 ^{+0.26} _{-0.21}	2.354	3% ± 2%	23.72 ^{+1.04} _{-0.52}	11.13 ^{+0.11} _{-0.09}	10.75 ^{+0.14} _{-0.13}	10.60 ^{+0.20} _{-0.34}
CID 255	1.625	19% ± 5%	0".19 ± 0".06	4.2 ± 1.5	21.61 ^{+0.37} _{-0.28}	2.858	4% ± 2%	22.89 ^{+0.60} _{-0.39}	11.03 ^{+0.15} _{-0.11}	10.65 ^{+0.18} _{-0.15}	10.48 ^{+0.23} _{-0.35}
CID 3242	2.751	46% ± 13%	0".20 ± 0".16	6.1 ± 1.9	21.16 ^{+0.35} _{-0.26}	2.596	5% ± 1%	23.60 ^{+0.34} _{-0.26}	11.12 ^{+0.14} _{-0.11}	10.75 ^{+0.17} _{-0.15}	10.62 ^{+0.19} _{-0.29}
CID 3570	1.665	77% ± 2%	0".70 ± 0".01	0.7 ± 0.1	21.16 ^{+0.02} _{-0.02}	1.332	86% ± 2%	22.97 ^{+0.01} _{-0.01}	10.98 ^{+0.02} _{-0.02}	10.71 ^{+0.10} _{-0.10}	9.78 ^{+0.68} _{-0.13}
CID 452	1.684	75% ± 4%	0".37 ± 0".02	1.4 ± 0.2	21.18 ^{+0.06} _{-0.06}	1.452	38% ± 1%	22.73 ^{+0.02} _{-0.02}	11.13 ^{+0.03} _{-0.03}	10.86 ^{+0.10} _{-0.10}	10.13 ^{+0.48} _{-0.29}
CID 454	2.203	36% ± 3%	0".39 ± 0".02	0.6 ± 0.1	21.20 ^{+0.08} _{-0.07}	1.291	9% ± 1%	23.35 ^{+0.06} _{-0.06}	11.07 ^{+0.04} _{-0.04}	10.70 ^{+0.10} _{-0.10}	9.77 ^{+0.74} _{-0.15}
CID 50	5.576	17% ± 9%	0".16 ± 0".11	3.2 ± 2.2	20.93 ^{+0.86} _{-0.48}	4.940	5% ± 3%	22.50 ^{+1.15} _{-0.55}	11.07 ^{+0.35} _{-0.19}	10.80 ^{+0.36} _{-0.21}	10.51 ^{+0.41} _{-0.56}
CID 543	1.902	31% ± 10%	0".10 ± 0".00	0.5 ± 0.3	21.99 ^{+0.41} _{-0.30}	1.435	5% ± 2%	23.77 ^{+0.53} _{-0.36}	10.70 ^{+0.19} _{-0.12}	10.43 ^{+0.54} _{-0.15}	9.55 ^{+0.64} _{-0.24}
CID 597	1.565	42% ± 17%	0".17 ± 0".06	1.8 ± 0.8	21.87 ^{+0.54} _{-0.36}	1.254	12% ± 1%	23.56 ^{+0.13} _{-0.11}	10.73 ^{+0.22} _{-0.15}	10.46 ^{+0.24} _{-0.18}	9.98 ^{+0.44} _{-0.49}
CID 607	1.692	44% ± 18%	0".21 ± 0".09	3.4 ± 1.1	21.19 ^{+0.58} _{-0.37}	2.590	5% ± 2%	23.57 ^{+0.51} _{-0.35}	11.02 ^{+0.23} _{-0.15}	10.75 ^{+0.25} _{-0.18}	10.57 ^{+0.29} _{-0.41}
CID 70	2.041	20% ± 5%	0".42 ± 0".10	3.6 ± 1.0	21.86 ^{+0.30} _{-0.24}	2.361	2% ± 1%	24.63 ^{+0.68} _{-0.41}	10.93 ^{+0.12} _{-0.10}	10.55 ^{+0.16} _{-0.14}	10.38 ^{+0.22} _{-0.34}
LID 1273	1.697	53% ± 9%	0".30 ± 0".04	1.2 ± 0.5	20.94 ^{+0.21} _{-0.18}	2.137	6% ± 1%	23.29 ^{+0.15} _{-0.13}	11.27 ^{+0.09} _{-0.07}	10.89 ^{+0.13} _{-0.12}	10.13 ^{+0.58} _{-0.28}
LID 1538	2.362	44% ± 8%	0".18 ± 0".04	2.8 ± 0.5	21.25 ^{+0.22} _{-0.18}	2.173	8% ± 1%	23.09 ^{+0.19} _{-0.16}	11.09 ^{+0.09} _{-0.08}	10.71 ^{+0.13} _{-0.12}	10.52 ^{+0.22} _{-0.37}
LID 360	3.918	18% ± 2%	0".63 ± 0".02	0.8 ± 0.4	21.46 ^{+0.14} _{-0.12}	4.914	4% ± 1%	23.25 ^{+0.17} _{-0.15}	11.04 ^{+0.06} _{-0.05}	10.66 ^{+0.11} _{-0.11}	9.76 ^{+0.65} _{-0.16}
XID 2138	1.597	39% ± 6%	0".50 ± 0".03	1.2 ± 0.4	21.87 ^{+0.17} _{-0.15}	2.731	5% ± 1%	23.90 ^{+0.31} _{-0.24}	10.85 ^{+0.07} _{-0.06}	10.48 ^{+0.12} _{-0.12}	9.71 ^{+0.57} _{-0.28}
XID 2202	3.23	33% ± 8%	0".10 ± 0".00	4.0 ± 1.0	21.16 ^{+0.30} _{-0.24}	3.852	8% ± 2%	22.59 ^{+0.29} _{-0.23}	11.11 ^{+0.12} _{-0.10}	10.74 ^{+0.16} _{-0.14}	10.58 ^{+0.21} _{-0.33}
XID 2396	3.669	24% ± 11%	0".58 ± 0".09	0.8 ± 1.4	21.40 ^{+0.65} _{-0.40}	5.346	2% ± 1%	23.36 ^{+0.24} _{-0.20}	11.07 ^{+0.26} _{-0.16}	10.69 ^{+0.28} _{-0.19}	10.00 ^{+0.58} _{-0.40}
CDFS-1	1.358	65% ± 20%	0".14 ± 0".07	4.8 ± 1.1	22.47 ^{+0.40} _{-0.29}	10.66 ^{+0.16} _{-0.12}	10.29 ^{+0.19} _{-0.15}	10.14 ^{+0.22} _{-0.31}
CDFS-229	4.329	18% ± 2%	0".51 ± 0".03	0.5 ± 0.2	21.57 ^{+0.14} _{-0.13}	10.90 ^{+0.06} _{-0.05}	10.63 ^{+0.12} _{-0.11}	9.71 ^{+0.70} _{-0.16}
CDFS-321	3.998	25% ± 12%	0".38 ± 0".12	2.3 ± 2.0	20.34 ^{+0.70} _{-0.42}	11.48 ^{+0.28} _{-0.17}	11.10 ^{+0.30} _{-0.20}	10.72 ^{+0.42} _{-0.58}
CDFS-724	1.355	35% ± 15%	0".12 ± 0".03	1.6 ± 1.1	23.70 ^{+0.58} _{-0.38}	10.06 ^{+0.23} _{-0.15}	9.79 ^{+0.25} _{-0.18}	9.25 ^{+0.48} _{-0.48}
ECDFS-358	2.012	56% ± 14%	0".36 ± 0".04	1.7 ± 0.5	21.34 ^{+0.30} _{-0.24}	11.11 ^{+0.12} _{-0.10}	10.73 ^{+0.16} _{-0.14}	10.22 ^{+0.44} _{-0.47}
SXDS-X1136	1.937	41% ± 8%	0".10 ± 0".00	2.0 ± 0.5	21.92 ^{+0.23} _{-0.19}	10.75 ^{+0.09} _{-0.08}	10.49 ^{+0.14} _{-0.13}	10.10 ^{+0.36} _{-0.48}
SXDS-X50	1.423	41% ± 9%	0".19 ± 0".04	1.7 ± 0.6	21.99 ^{+0.27} _{-0.21}	10.80 ^{+0.11} _{-0.09}	10.54 ^{+0.15} _{-0.13}	10.01 ^{+0.45} _{-0.46}
SXDS-X717	1.426	61% ± 9%	0".26 ± 0".07	5.6 ± 1.4	21.76 ^{+0.18} _{-0.15}	10.77 ^{+0.07} _{-0.06}	10.51 ^{+0.12} _{-0.12}	10.38 ^{+0.18} _{-0.29}
SXDS-X735	2.203	32% ± 9%	0".22 ± 0".06	2.0 ± 1.0	20.92 ^{+0.33} _{-0.25}	11.16 ^{+0.13} _{-0.10}	10.78 ^{+0.17} _{-0.14}	10.42 ^{+0.36} _{-0.56}
SXDS-X763	2.376	6% ± 4%	0".69 ± 0".53	2.4 ± 0.8	24.13 ^{+1.17} _{-0.55}	9.95 ^{+0.47} _{-0.24}	9.68 ^{+0.48} _{-0.24}	9.35 ^{+0.48} _{-0.56}
SXDS-X969	1.613	29% ± 11%	0".11 ± 0".02	2.1 ± 1.1	21.59 ^{+0.52} _{-0.35}	10.99 ^{+0.21} _{-0.14}	10.61 ^{+0.23} _{-0.17}	10.21 ^{+0.40} _{-0.54}

Note. Column 1: object ID. Columns 2–6: WFC3 inference. The reduced χ^2 value corresponds to the inference by the best PSF in the library. Columns 7–9: ACS inference. Column 10: observed host luminosity in the rest-frame R band. Column 11: host total stellar mass. Column 12: bulge stellar mass, using Sérsic index as B/T proxy; see Section 5.6 for details.

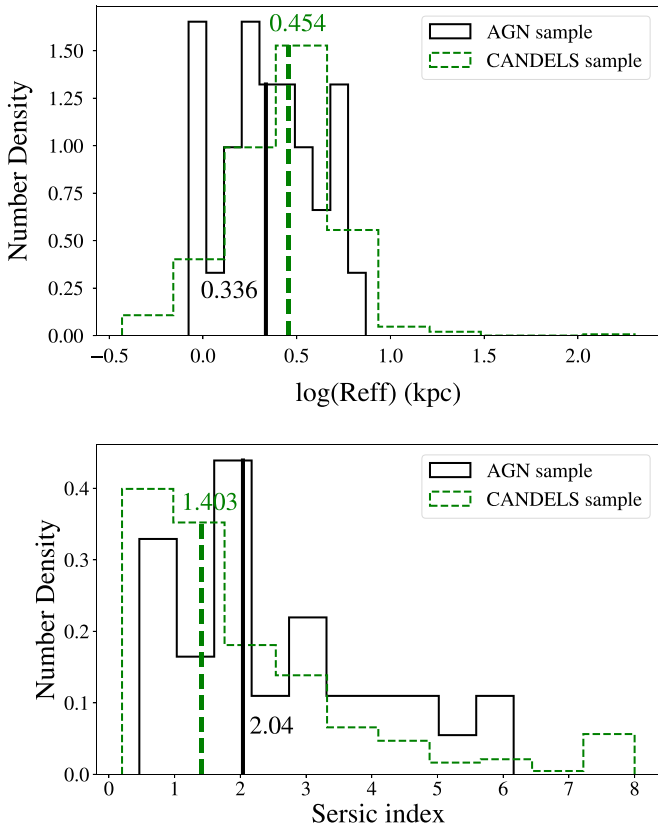


Figure 4. Comparison of the histogram of the R_{eff} (top panel) and Sérsic n_s (bottom panel), with median value indicated. For comparison, we show the distribution of CANDELS galaxies at similar redshifts and stellar masses to our type 1 AGN sample.

The distributions of effective radius R_{eff} are shown in Figure 3 (bottom panel). Based on the redshift, we calculate the physical scale of the radius for each object in kpc assuming a standard cosmology. We plot them together with the measured Sérsic index in Figure 4. These values are distributed within the allowed range and not concentrated on either the upper or lower bound. The R_{eff} values of our sample are between ~ 1 and 7 kpc (peaked at ~ 2.2 kpc). Nearly half (15/32) of our systems have a Sérsic index $n < 2$, indicating that they have a significant disk component, likely in addition to the presence of a bulge. Five systems have a high Sérsic index ($n > 4.5$) for the first run; we use $n \in [1, 4]$ as a prior to refit these systems and find that the changes on the inference of their host luminosity are very limited (< 0.03 dex). Seven systems have an effective radius $R_{\text{eff}} < 0''.18$, i.e., smaller than 3 pixels. In order to check whether this affects our conclusions, we refit them with an $R_{\text{eff}} \in [0''.2, 1''.0]$ prior and find that the inferred host flux barely changes ($< 1\%$). In particular, the inferred R_{eff} for three systems (CID 543, XID 2202, and SXDS-X1136) hit the lower limit (i.e., $0''.1$); thus, the scatter on the parameter is formally zero. This means that the size inference of these three systems should really be considered an upper limit, rather than a measurement. However, the inferences of their host luminosities and stellar masses are still reliable given the consistency of the refitting results and the small scatter in the host flux ($< 10\%$).

We compare the morphology of AGN host galaxies to inactive galaxies from the CANDELS survey (Grogin et al. 2011; Koekemoer et al. 2011). We identify 4401 inactive

galaxies within a redshift range ($1.2 < z < 1.7$), comparable to our AGN sample, whose Sérsic measurements are provided by van der Wel et al. (2012) using GALFIT. Their stellar masses are derived based on the 3D-*HST* spectroscopic survey (Brammer et al. 2012; Momcheva et al. 2016) and comparable to our AGN hosts ($9.5 < \log(M_*/M_\odot) < 11.5$; Section 5.4). We compare the histogram of the inferred R_{eff} and Sérsic index to the inactive galaxies in Figure 4, where we find no significant difference between their distributions and median value. We also test whether the distributions can be drawn from the same parent population using a Kolmogorov–Smirnov test and determining the p -value to be 0.42 and 0.04 for R_{eff} and n , respectively. We conclude that the host galaxies of our AGN sample are representative of the overall population of galaxies, with a significant disk component, at comparable luminosity and stellar mass at the same redshift. In Section 5.6, we use this information to infer the likely bulge masses, hence the $\mathcal{M}_{\text{BH}}-M_{*,\text{bulge}}$ relation.

5.2. Rest-frame Colors

For 21/32 AGNs, we have multiband host magnitudes that enable us to select the appropriate stellar population templates to determine rest-frame luminosities and stellar masses for the overall sample. We find that the 1 and 0.625 Gyr stellar populations with solar metallicity and a Chabrier IMF (Bruzual & Charlot 2003) provide excellent matches to the observed colors of our sample at $z < 1.44$ and $z > 1.44$, respectively (see Figure 5). To minimize the uncertainty associated with these corrections, we use these two templates to interpolate to the rest-frame R band, which is very close to the observed wavelengths. We note that the choice is not unique, and other combinations of ages, metallicities, and star formation history could match the observed colors and would provide very similar R -band magnitudes, as well as stellar masses (Bell & de Jong 2000, 2001).

5.3. $\mathcal{M}_{\text{BH}}-L_{\text{host}}$ Relation

Adopting the 1 and 0.625 Gyr stellar populations, we perform a K-correction to derive the rest-frame R -band magnitude of our sample, based on the host inference in the WFC3 band. As mentioned above, since the WFC3 filter is already close to the rest-frame R band, we expect the M_R uncertainty introduced by this K-correction to be within 0.05 mag. We derive the rest-frame R -band luminosity from $\log L_R/L_{R,\odot} = 0.4 \times (M_{R,\odot} - M_R)$, where $M_{R,\odot} = 4.61$ (Blanton & Roweis 2007). Here L_R ranges between $\log(L_R/L_{R,\odot}) \in [9.5, 11.5]$ with individual values listed in Table 4.

We show the relation between \mathcal{M}_{BH} and L_{host} in Figure 6 with comparison samples. For reference, we fit the local data with a linear relation,

$$\log\left(\frac{\mathcal{M}_{\text{BH}}}{10^7 M_\odot}\right) = \alpha_0 + \beta_0 \log\left(\frac{L_R}{10^{10} L_\odot}\right), \quad (7)$$

which enables a direct comparison between our high- z sample and the local relation. The distribution of our data appears to be in good agreement with the local relation and the other AGN samples at lower redshift. Therefore, the observational data indicate that the relation between black hole mass and host luminosity are similar at different periods of the universe. In

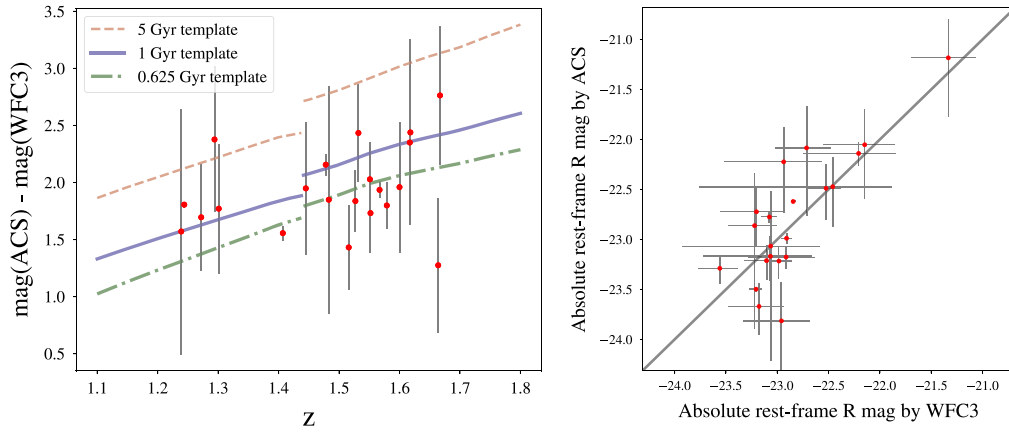


Figure 5. Left: observed color as a function of redshift, based on 21/32 AGNs that have both WFC3 and ACS imaging data. Note that the filter combinations WFC3/F125W and WFC3/F140W are adopted for galaxies at $z < 1.44$ and $z > 1.44$, respectively. We also plot three predicted models including 5, 1, and 0.625 Gyr. Clearly, the 5 Gyr stellar population is ruled out by our data, and we adopt the 1 and 0.625 Gyr for galaxies at $z < 1.44$ and $z > 1.44$, respectively. Right: comparison of the inferred rest-frame R -band magnitude, based on the adopted stellar populations.

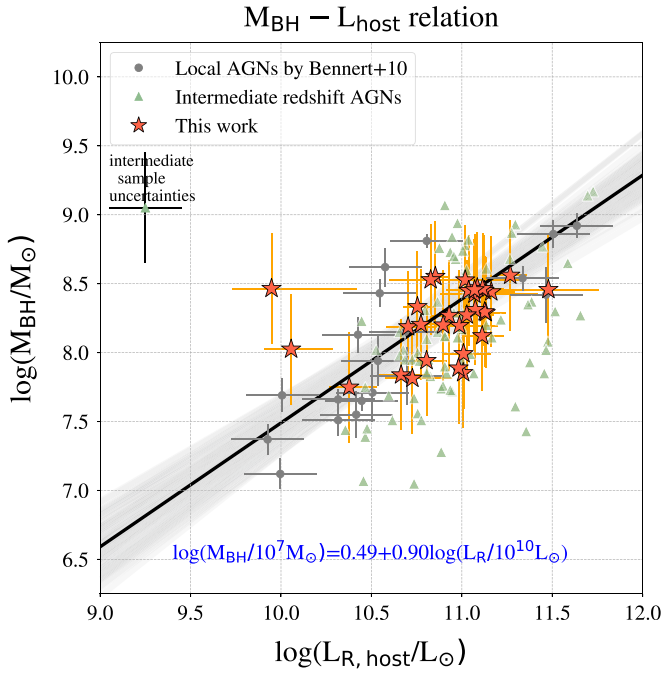


Figure 6. Observed black hole mass vs. R -band luminosity relation. The black line and blue equation indicate the best-fit result of the local sample as given in Equation (7), with a 1σ confidence interval indicated by the gray shaded region. The values for the comparison samples at low and intermediate redshift are listed in Tables 1 and 2 of Ding et al. (2017b).

Appendix A, we explore how the high- z sample would evolve in this plane solely with the luminosity evolution of the host galaxy as done in past studies (e.g., Ding et al. 2017b).

We note that there are outliers that deviate from the distribution of the overall sample, such as SXDS-X763. We suspect that this source may have abnormal host properties. Indeed, the value of R_{eff} has a large uncertainty ($\sim 75\%$), and the host-to-total flux ratio is the lowest of the high- z sample ($< 10\%$).

5.4. $M_{\text{BH}}-M_*$ Relation

Using the near-IR imaging with *HST*, we take the host luminosity along with color information to estimate the stellar

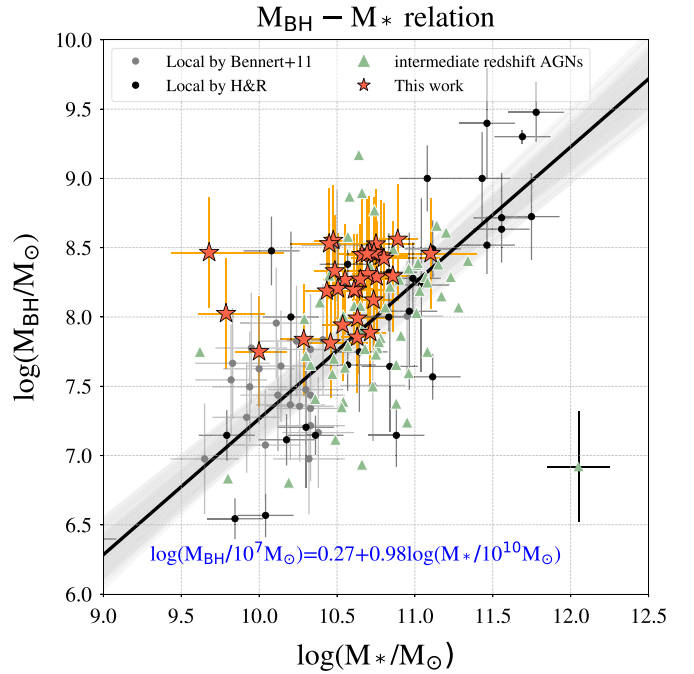


Figure 7. Black hole mass vs. stellar mass relation ($M_{\text{BH}}-M_*$). The best-fit local relation is shown as described in Figure 6.

mass content of each host galaxy based on the mass-to-light ratio of the adopted stellar populations. The uncertainty level associated with the stellar mass is expected to be of order 0.1 dex (changing the IMF would affect all of our stellar masses systematically). We find that M_* ranges between $\log(M_*/M_\odot) \in [9.7, 11.3]$. These values are listed in Table 4.

In Figure 7, we plot our $M_{\text{BH}}-M_*$ measurements and find that the distributions in this plane for the four samples are similar. However, there is a slight shift of the high- z data toward higher black hole masses at a fixed host mass. In Figure 8, we plot the mass ratio as a function of redshift (right panel) and the mass ratio difference ($\Delta \log M_{\text{BH}} = \log\left(\frac{M_{\text{BH}}}{10^7 M_\odot}\right) - \alpha - \beta \log\left(\frac{M_*}{10^{10} M_\odot}\right)$, which is considered as the difference between the high-redshift data and the best-fit local relation; left panel). For our high- z sample, we find the averaged $\Delta \log M_{\text{BH}}$ to be 0.43 ± 0.06 , a

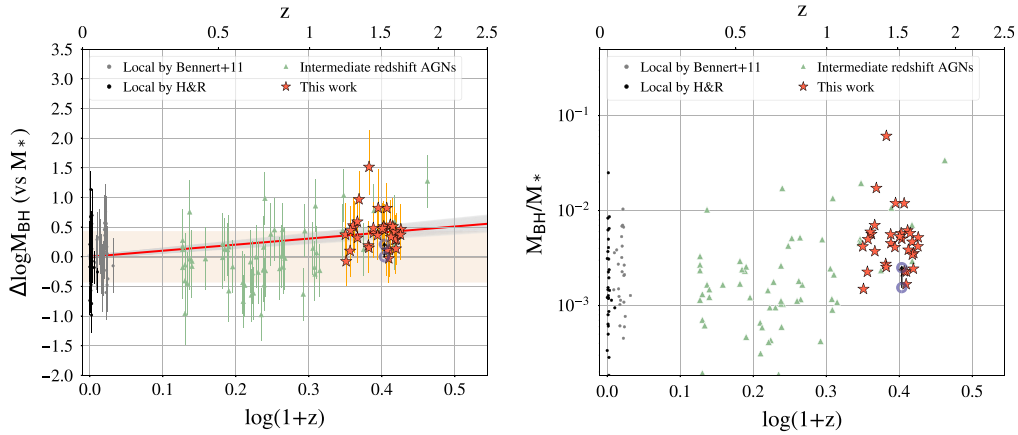


Figure 8. Left: offset in $\log(\mathcal{M}_{\text{BH}})$ (vs. M_*) as a function of redshift. The orange band is the intrinsic scatter of the local linear relation. The red line and gray shaded region are the best-fit and 1σ offset fitting by Equation (9) using our 32 high- z AGNs, with slope value $\gamma = 1.03 \pm 0.25$. Right: $\mathcal{M}_{\text{BH}}/M_*$ as a function of redshift. In both panels, we use blue open circles to show the expected bias of the median value for $\Delta \log \mathcal{M}_{\text{BH}}$. We use the framework of Schulze & Wisotzki (2011, 2014) to show that even with no evolution, the selection effects would shift the expectation higher toward the measured values, as indicated by the small arrow (Section 2.3.) The measurements of the local and intermediate-redshift samples are recalibrated using self-consistent recipes and listed in Table 7.

factor of ~ 2.7 higher than the local mass ratio, as indicated by the top blue circle in Figure 8.

As with Equation (7), we fit the $\mathcal{M}_{\text{BH}}-M_*$ data with a linear relation as

$$\log\left(\frac{\mathcal{M}_{\text{BH}}}{10^7 M_\odot}\right) = \alpha_1 + \beta_1 \log\left(\frac{M_*}{10^{10} M_\odot}\right) \quad (8)$$

and an evolution term parameterized in the following form:

$$\Delta \log \mathcal{M}_{\text{BH}} = \gamma \log(1+z). \quad (9)$$

Performing such a fit based on the observed data (i.e., no correction for selection effects), we obtain $\gamma = 1.03 \pm 0.25$. Even with the exclusion of the few outliers, the slope is significantly nonzero with $\gamma = 0.89 \pm 0.27$. The best-fit observed evolution model is shown in Figure 8.

As shown in these panels, the scatter of the high- z correlation presents a similarity to the local relation. To quantitatively make this comparison, we investigate the intrinsic scatter of our sample. Note that the observed high- z sample has effects from both the measurement uncertainty and the narrow selection window, and thus one needs to take them both into account to extract the intrinsic scatter. Based on our forward-modeling framework, we find that our AGN sample has intrinsic scatter as 0.25 dex on the vertical axis, taking into account the measurement uncertainty and the selection function. We will return to this topic in a forthcoming paper (X. Ding et al. 2019, in preparation), where we focus on the scatter of the sample as a diagnostic of the AGN–host galaxy feedback mechanism. The fact that the intrinsic scatter for the high- z sample is no larger than the local one, which is ~ 0.35 dex (Gültekin et al. 2009), may pose a challenge for explanations of scaling relations where random mergers are the origin of the correlation (Peng 2007; Jahnke & Macciò 2011), indicating that there may likely be a connection between the SMBHs and their host galaxies during their formation.

5.5. Taking into Account the Selection Function

In Section 2.3, we used the Bayesian framework introduced by Schulze & Wisotzki (2011) and found that in the case of no intrinsic evolution of the correlations, we would expect to measure an offset corresponding to a $+0.21$ dex bias in the

inferred $\Delta \log \mathcal{M}_{\text{BH}}$, owing to our selection function. Interestingly, this bias could account for the majority of the observed offset as obtained in the $\mathcal{M}_{\text{BH}}-M_*$ correlations in the last section. To demonstrate, we use blue open circles to show the expected bias raised by this selection effect in Figure 8. We also show, in Figure 9, the histogram $\Delta \log \mathcal{M}_{\text{BH}}$ of the high- z sample and compare it to the local ones. The plots show that the correlations between \mathcal{M}_{BH} and host galaxy total stellar mass or luminosity could be consistent with those of the local samples, given the uncertainties and selection function.

To further evaluate the “true” underlying evolution and its uncertainty, corrected for selection effects and taking into account the actual observations, we adopt an independent method based on the approach introduced by Treu et al. (2007) and developed by Bennert et al. (2010), Park et al. (2015), and Ding et al. (2017b). The method parameterizes the evolution of the correlations between \mathcal{M}_{BH} and host properties as an offset from the local γ and an intrinsic scatter σ_{int} , which can be a free parameter or tied to the local relation. It then imposes a selection function in \mathcal{M}_{BH} and calculates the intrinsic parameters of the model given the observations. In practice, we start from the local black hole mass function and the evolution model, generate mock samples using a Monte Carlo approach, apply the selection function, and compare with the data to generate the likelihood. To illustrate the importance of the intrinsic scatter in the selection effects, we adopt both a uniform (flat) prior and a lognormal prior for σ_{int} . Note that this method assumes a narrow Eddington ratio distribution, which is different from the one by Schulze & Wisotzki (2011), as described in Section 2.3. Also, this method adopts the local black hole mass function rather than the high- z black hole mass function. These differences have a second-order effect and could be responsible for the different magnitude of the selection effect. On the other hand, this method probes the importance of the scatter at high- z , which is complementary.

Combining the 32 AGNs together with the intermediate-redshift sample, we present the inferred γ and σ_{int} in the two-dimensional planes in Figure 10. The plots show that the inferred evolution is uncertain and depends crucially on the intrinsic scatter, especially when applying a luminosity evolution for the host (see Appendix A). Assuming the lognormal prior σ_{int} , to mimic the assumption of the method

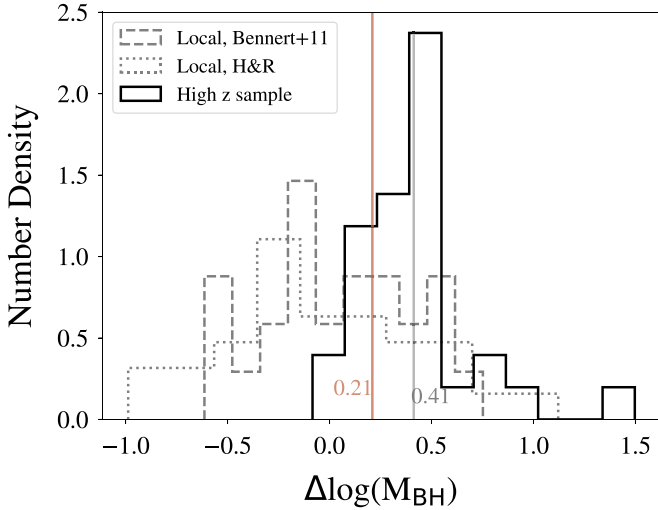


Figure 9. Histogram of the $\log(\mathcal{M}_{\text{BH}})$ offset for the local samples and our 32 high- z samples. The gray vertical line shows the mean value of the offset for the high- z sample, and the red vertical line shows the shift in the expectation by the selection effect, even if there were no evolution. The median value of the offset is very close to the mean value (+0.30).

discussed in Section 2.3, one sees that the best estimate of γ is positive, but the 95% confidence intervals extend to zero. Thus, one cannot conclude that evolution is significantly detected in our data. When relaxing the prior on σ_{int} , we find that the scatter is consistent with being as low as in the local samples, with a one-sided interval including zero and 1σ upper limit at around 0.5 dex. We also study the selection effect by only considering the 32 new AGNs, resulting in a higher evolutionary trend with a higher value of γ . We show the results of γ and σ_{int} in Table 5.

A simple check using our prior estimate of the bias yields a similar result. The mean offset of the sample of 32 objects from the local relationship is 0.43 ± 0.06 dex, which would correspond to $\gamma = 1.08 \pm 0.15$. However, after correcting for the selection bias (0.21 dex; see Section 2.3), the offset reduces to 0.22 ± 0.06 and thus $\gamma = 0.55 \pm 0.15$, marginally positive but not conclusively inconsistent with the local value given the error bars and uncertainty in the correction. We also note that the distribution of offsets shown in Figure 9 displays a positive asymmetric tail. We expect the negative tail to be suppressed by our selection function, and thus it should be accounted for in our treatment. If one computes the median offset instead of the mean, the offset is almost completely consistent with the expected bias. Larger samples with different selection functions are needed to establish whether the positive tail is real or due to small sample statistics.

5.6. $\mathcal{M}_{\text{BH}}-M_{*,\text{bulge}}$ Relation

The local sample of inactive galaxies used in this analysis is mainly comprised of bulge-dominated galaxies, and the entire local M_* we adopted is their bulge masses. That is, in previous sections, we are comparing the $\mathcal{M}_{\text{BH}}-M_{*,\text{total}}$ relations in the distant universe to the $\mathcal{M}_{\text{BH}}-M_{*,\text{bulge}}$ relations locally. Considering that a significant stellar component of the high- z AGNs have a disk component (i.e., AGN hosts with fitted Sérsic index close to 1), $M_{*,\text{bulge}}$ must be smaller than $M_{*,\text{total}}$. Given that the structures of our AGN hosts are similar to inactive galaxies at equivalent redshifts and stellar masses (Section 5.1), we expect their B/T ratios to follow a similar

Table 5
Summary of γ Inferences

Sample	Selection Effects	$\mathcal{M}_{\text{BH}}-M_*$	$\mathcal{M}_{\text{BH}}-L_{\text{host}}$
32 AGNs + intermediate	No	0.72 ± 0.20	0.64 ± 0.17
32 AGNs + intermediate	Yes	0.90 ± 0.40	0.50 ± 0.50
32 AGNs	No	1.03 ± 0.25	1.07 ± 0.23
32 AGNs	Yes	1.50 ± 0.80	1.80 ± 0.80

Note. The entire sample includes the 32 AGNs and intermediate-redshift AGNs from the reference in Section 2.4. Note that the adopted L_{host} has been transferred to today, assuming the passive evolution scenario using Equation (10). The results of selection effects used the uniform (flat) prior of σ_{int} .

distribution that can be estimated using a single Sérsic index (Bruce et al. 2014). We can then infer the bulge stellar mass of our AGN hosts based on the inferred B/T ratios.

First, we establish a relation between the single Sérsic index and the B/T ratio using inactive galaxies from CANDELS at similar redshifts and stellar masses (Figure 11; $\log(M_*/M_\odot) \in [9.0, 11.5]$) using the B/T measurements of Dimauro et al. (2018). In the figure, the red line indicates the average B/T ratio at a given Sérsic index. We then implement a Monte Carlo approach by randomly sampling a Gaussian Sérsic distribution for each AGN in our sample based on our measurements with 1σ errors (Table 4). Next, we randomly sample the associated B/T ratio for a given Sérsic index. To avoid the case of an unphysical faint bulge flux, we set the lower limit for the B/T ratio as 0.1. In each realization, we compare the $M_{*,\text{bulge}}$ to the \mathcal{M}_{BH} and estimate the offset and γ . We use 10,000 realizations to make sure the distribution of random samples is stable. Note that the Monte Carlo approach would take the scatter into account, including the Sérsic index and its relation with the B/T ratio. We list the resulting bulge masses $M_{*,\text{bulge}}$ in Table 4.

As expected, we find a stronger offset of $\Delta \log \mathcal{M}_{\text{BH}}^{\text{bulge}} = 0.87 \pm 0.07$ dex in $\mathcal{M}_{\text{BH}}/M_{*,\text{bulge}}$ with respect to the local relation, which corresponds to an evolutionary trend with $\gamma = 2.09 \pm 0.30$. Since selection effects are independent of B/T in our framework, we can apply our prior estimate of the correction for selection effects by removing 0.21 dex, still leaving a significant offset of 0.67 ± 0.07 dex. We show the histogram of $\mathcal{M}_{\text{BH}}/M_*$ and γ inferred by the Monte Carlo approach in Figure 12 and illustrate the offset between bulge and black hole as a function of redshift in Figure 13.

Even with the uncertainty associated with our estimate of the bulge-to-total ratio, it is clear that there is a significant evolution in the $\mathcal{M}_{\text{BH}}-M_{*,\text{bulge}}$ relation, considering the marginal evidence for evolution in the $\mathcal{M}_{\text{BH}}-M_{*,\text{total}}$ relation and that our galaxies are not pure bulges. This finding confirms with higher fidelity the conclusion by Bennert et al. (2011b) based on optical data of a smaller sample of 11 objects in the same redshift range (see Jahnke et al. 2009; Cisternas et al. 2011; Schramm & Silverman 2013, for similar results). We list the inferred γ using the different sample combinations in this section in Table 6.

6. Final Technical Remarks

6.1. Systematic Errors

In this work, we use state-of-the-art techniques to measure the host galaxy flux, separating it from that of the point source. The

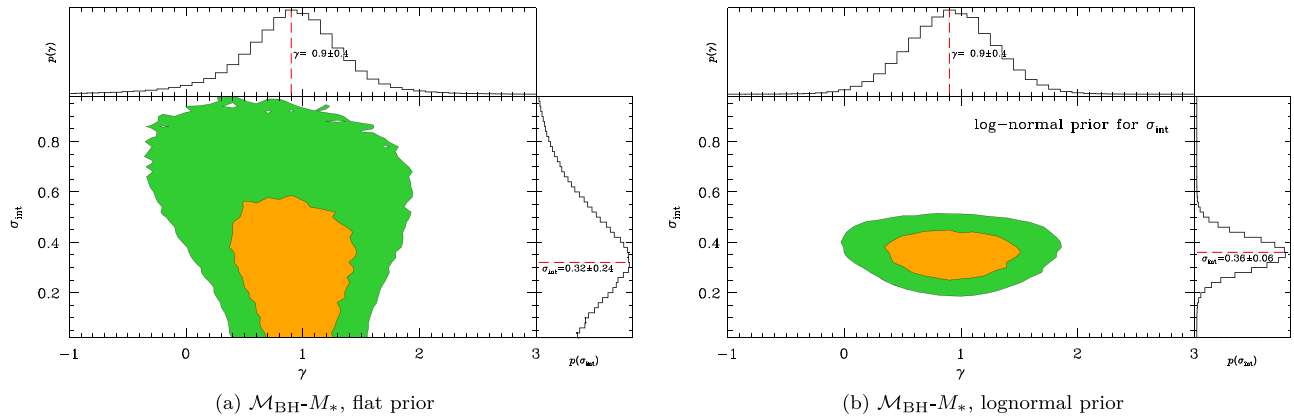


Figure 10. Constraining the evolution factor γ of the $\mathcal{M}_{\text{BH}}-M_*$ relation (Equation (9)), with intrinsic scatter σ_{int} , using a Monte Carlo simulation. The adopted sample includes our 32 AGNs and the intermediate-redshift AGNs using a flat prior of σ_{int} (left panel) and lognormal prior (right panel). The colored regions indicate the 68% and 95% confidence regions.

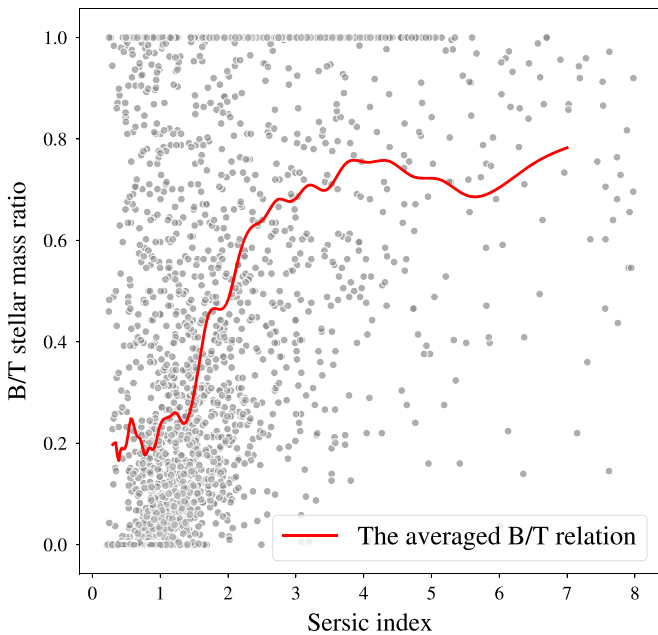


Figure 11. Relation between bulge-to-total stellar mass ratio and single Sérsic index using CANDELS inactive galaxies with $\log(M_*/M_\odot) \in [9.0, 11.5]$. The red curve is the averaged B/T ratio at a different Sérsic index. Note that this curve is only for demonstrating the expected B/T value at a different Sérsic index. In this work, we adopt the Monte Carlo approach to randomly sample the B/T to account for the scatter.

fidelity of the host galaxy magnitude is high, as demonstrated by the robustness with respect to the choice of PSF, which is the primary source of uncertainty. However, we introduce some uncertainty by adopting two common simple stellar population templates to derive the rest-frame R -band luminosity and stellar mass for the full population. In principle, if we had more information on the color, we could improve on this source of uncertainty by adopting a specific stellar population model for each target. However, considering that the host magnitude in the HST/ACS band is faint (host-to-total flux ratio $<30\%$), the individual color that we measure is insufficient to further discriminate between templates; thus, we adopt the common templates for simplicity and to facilitate reproduction of our work.

In any case, we stress that the uncertainty in the scaling relations is dominated by single-epoch black hole mass estimates

Table 6
Observed γ for $\mathcal{M}_{\text{BH}}-M_*$ without Selection Effect Corrections

Sample Combination	γ
32 AGNs	1.03 ± 0.25
30 AGNs (excluded outliers)	0.89 ± 0.27
32 AGNs + intermediate	0.72 ± 0.20
32 AGNs bulge only	2.09 ± 0.30

Note. These values are directly inferred for the observation, without corrections due to selection effects.

(i.e., 0.4 dex), and not by uncertainties in the photometry or stellar mass estimates (i.e., typically ~ 0.15 dex). Thus, the choice of template is a subdominant source of error. Note that the large uncertainties of \mathcal{M}_{BH} are not immediately apparent from the figures, since only the AGNs that have measured \mathcal{M}_{BH} that falls into our selection window (i.e., $\log(\mathcal{M}_{\text{BH}}/M_\odot) \in [7.5, 8.56]$) have been selected. A posteriori, the fact that the intrinsic scatter we observe is not larger than the one in the local universe is consistent with this statement.

6.2. Systematic Errors Related to the Choice of Local Anchor

To compare our high- z sample to the local relation, we adopt the local measurements by Bennert et al. (2010, 2011a) and Häring & Rix (2004). In the literature (Kormendy & Ho 2013; hereafter K13; Bentz & Manne-Nicholas 2018), other analyses of the local sample are available, which could also be considered as the local anchor. However, from the point of view of our differential evolutionary measurement, we stress once again the importance of selecting local anchors that have been measured and calibrated in a similar way to the distant high- z samples. It is crucial that the black hole masses be obtained in the same of self-consistent manner, and it is also critical that the host/AGN decomposition be measured in the most similar way possible.

Therefore, for these reasons, the B10 and HR04 samples are the most appropriate for our goal, in spite of their limitations. For instance, B10 did not consider morphological features like strong bars in the decomposition. This choice might affect the inference of the bulge/disk properties in absolute terms, but it is the most similar decomposition to what is possible at high- z , where these features cannot be resolved. Also, the HR04

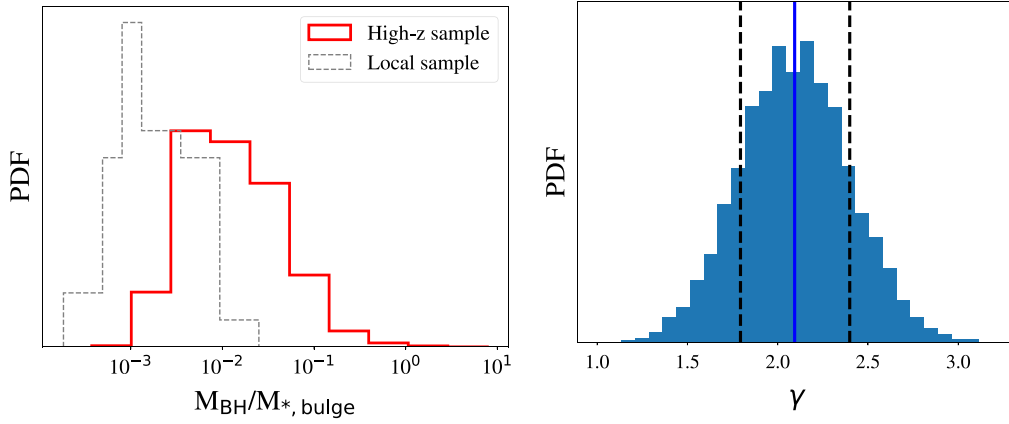


Figure 12. Illustration of the distribution from the 10,000 time realizations. Left: M_{BH}/M_* distribution for the 32 high- z sample, compared to the local one. Right: γ distribution, with median value (blue line) and 1σ region (dashed line).

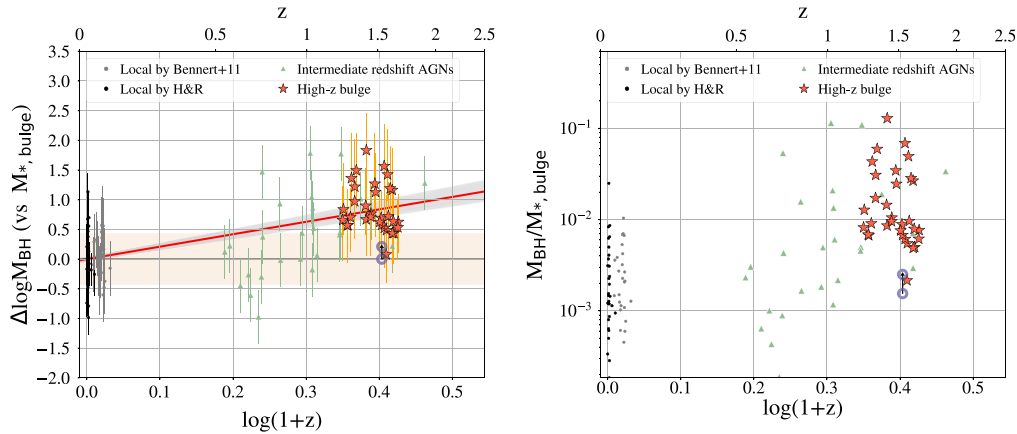


Figure 13. Same as Figure 8 but for the $M_{\text{BH}}-M_{*,\text{bulge}}$ relations. The intermediate sample consists of 27 objects from Bennert et al. (2011b) and Schramm & Silverman (2013), listed in Table 7. Cisternas et al. (2011) did not provide information to infer their bulge mass.

sample uses Jean modeling to estimate the M_* rather than using color information. This gives rise to systematic uncertainties related to the choice of the IMF, for example, which need to be kept in mind. We refer the reader to K13 for more discussion of systematic issues in local samples.

The issue of a consistent calibration of black hole masses is perhaps the most subtle and thorny. Not all of the local correlations are mutually consistent, especially when considering different galaxy properties, like luminosity, stellar mass, and velocity dispersion, and therefore a single self-consistent calibration is not possible. To illustrate the problem, we compare our local $M_{\text{BH}}-M_*$ sample to that published by K13. We find that the $M_{\text{BH}}-M_*$ measurements by K13 have a global $\sim +0.3$ dex offset relative to our local sample. Note that a $+0.3$ dex difference would almost erase the $\Delta \log M_{\text{BH}}$ for the high-redshift sample, as described in the last section, if it were independent of the black hole mass calibration. However, the $M_{\text{BH}}-\sigma_*$ relations by K13 are also offset by $\sim +0.3$ dex with respect to those given by Woo et al. (2010), which is the baseline for our adopted black hole mass estimators. That is, if we were to adopt the K13 normalization instead, the M_{BH} of all of the AGN sample should be increased by ~ 0.3 dex at the same time. As a result, adopting a different local anchor would only globally affect the level of M_{BH} to the local and high- z samples at the same time, with the result of leaving $\Delta \log M_{\text{BH}}$ unchanged. To illustrate this point further, we adopt the K13

local ellipticals and classical bulges as the $z \sim 0$ anchor and compare to the recalibrated M_{BH} of our high- z AGN sample. The inference of γ changes to 0.74 ± 0.31 , which is consistent at a 1σ level with the value (i.e., $\gamma = 1.03 \pm 0.25$) based on our chosen anchor.

Bentz & Manne-Nicholas (2018), given the superior resolution of their data in the local universe, decomposed their host using more components than bulge+disk (e.g., bar(s), barlens, ring(s)). This approach is impossible at high- z given current data; therefore, their sample should not be used as a local anchor, for consistency. Just for illustration, when adopting Bentz & Manne-Nicholas (2018) as the local anchor, we obtain $\gamma = 2.12 \pm 0.32$ using the 32 AGNs, still indicating a positive evolution, although, as expected, the amount of evolution is different for the reasons given above.

In conclusion, whereas the uncertainty in the local anchor does not affect our measurement of evolution, it is important to keep this issue in mind in evolutionary studies and verify that the measurements are as self-consistent as possible in the local and distant universe. In order to further reduce the uncertainty, one should perform a self-consistent measurement with identical techniques and data quality in both the local and distant universe. This effort is currently in progress and, when completed, should enable us to completely eliminate this source of uncertainty (Bennert et al. 2011b, 2015; Harris et al. 2012).

7. Conclusions

We studied the evolution of the correlations between the SMBHs and their host galaxies using new measurements of 32 X-ray-selected AGNs at $1.2 < z < 1.7$. Near-infrared spectroscopic observations with Subaru/FMOS of the $H\alpha$ emission line are available that provide reliable black hole masses. To obtain the properties of the AGN host galaxies, we performed an image decomposition using state-of-the-art techniques on *HST*/WFC3-IR data to obtain high-resolution imaging of the AGN and its host. This required us to collect PSF stars across all fields to build a library of PSFs. Using the state-of-the-art image modeling tool LENSTRONOMY, we decomposed the AGN image in the two-dimensional plane, taking each PSF in the library. We obtained the host properties (i.e., host flux, effective radius, Sérsic index) using a weighted arithmetic mean based on the inference from the eight top-ranked PSFs. With an additional *HST*/ACS image in the optical, we identified the appropriate stellar populations and derived the rest-frame *R*-band luminosity (L_{host}) and stellar mass (M_*) of the host with the corresponding mass-to-light ratio. We then determined the mass relations at high- z and established any signs of evolution by combining our high- z measurements with local and intermediate-redshift samples from the literature (Bennert et al. 2011b; Cisternas et al. 2011; Schramm & Silverman 2013; Park et al. 2015).

We find that the average “observed” ratio between the mass of an SMBH and either its total host luminosity or total stellar mass is larger at $z \sim 1.5$ by 0.41 (a factor of ~ 2.6) and 0.43 (a factor of ~ 2.7) dex, respectively, as compared to that in the local universe. However, taking into account uncertainties and the bias due to selection effects, the offset to the local universe is only marginally significant. Even with the remaining uncertainties in the corrections for selection, we are confident that any evolution in the $\mathcal{M}_{\text{BH}}/M_*$ relation is at most a factor of 2, with the case of no evolution entirely plausible.

Considering the bulge component (Woo et al. 2008; Bennert et al. 2011b) separately, we find that our high- z AGN sample has significantly lower mass/luminosity bulges at a fixed black hole mass than in the local universe. Comparing to their \mathcal{M}_{BH} , we find evolution with the ratio evolving as $(1+z)^{2.09 \pm 0.30}$, which is significant even when accounting for selection effects. We caution that the evolution of the bulge component is more uncertain than our measurement of the total galaxy components, since it is based on an estimate of the B/T ratio from the measured Sérsic index based on a matched sample of inactive galaxies. Nevertheless, since the signal is stronger than that for the integrated quantities, the measurement is more significant, even given larger uncertainties. Thus, we can conclude that the black holes 8–10 Gyr ago reside in bulges that are less massive/luminous than today (see also Bennert et al. 2011b; Park et al. 2015), even though a proper measure of the bulge mass at high- z may need to wait for the next generation of ground-based 20–30 m class telescopes.

We summarize several limitations of this work. First, due to the finite resolution of the *HST*, we model the host as a single Sérsic profile. The residuals do not show evidence of additional components, indicating that our choice is appropriate given the noise and resolution of the data. However, we cannot exclude that more features would be revealed by higher-quality data.

Second, we adopt simple stellar population templates to derive the host luminosity and stellar mass for the sample, which introduces some uncertainty in the inference of the host

properties. However, this source of uncertainty is subdominant with respect to that associated with single-epoch black hole mass estimates (see Section 6.1 for details).

Third, for a few AGN hosts, their inferred host effective radius hits the lower limit, and thus the inference of their R_{eff} should be considered as the upper limit. However, the inference of the host luminosity and stellar mass is still reliable in these cases, as shown by our test using different lower limit boundaries (Section 5.1).

Fourth and last, the choice of local anchor affects our inferred evolution at some level. We adopted as our baseline the local samples for which measurements have been made with a procedure that is most similar to the one we have applied at high- z , but other choices are possible. We investigated the impact of different choices for the local anchor in detail, and we found that even though the numerical values can change somewhat, the inferred evolution is always positive (see Section 6.2).

Given that the $M_{*,\text{total}}-\mathcal{M}_{\text{BH}}$ relation is closer to or consistent with the local relation, the inferred evolution of the $M_{*,\text{bulge}}-\mathcal{M}_{\text{BH}}$ correlations is qualitatively consistent with a scenario where the assembly of the black hole predates that of the bulge, which is processed by the transfer of stellar mass from the disk via mergers or secular processes (Jahnke et al. 2009; Bennert et al. 2011a; Schramm & Silverman 2013). The stellar mass needed to build the bulge appears to be present in the disk component at high- z .

Of further interest, the scatter in the $\mathcal{M}_{\text{BH}}-M_*$ ratios at high- z is similar to the local one. This was unexpected, since the measurements of the masses of both the black holes and their hosts should have more uncertainty than local estimates. If true, this may indicate that cosmic averaging of initially unrelated states (Peng 2007) is not driving the relation between SMBHs and their host galaxies, since then a larger scatter at higher redshifts would be expected. Thus, there is likely a connection between the two yet to be fully understood; contenders include AGN feedback or links to common gas reservoirs.

Finally, the forthcoming launch of the *James Webb Space Telescope* and the first light of adaptive optics–assisted extremely large telescopes may provide high-quality imaging data of AGNs at higher redshift (up to $z \sim 7$) and thus trace the evolution of correlations at the more distant universe. Although galaxies, as we know, are smaller at high- z , so it thus may remain challenging to detect under the glare of a luminous AGN. In the lower-redshift universe, wide-area surveys with Subaru/HSC, LSST, and *WFIRST* offer much promise to build samples for studying these mass ratios and dependencies on other factors (e.g., environment).

Based in part on observations made with the NASA/ESA *Hubble Space Telescope*, obtained at the Space Telescope Science Institute, which is operated by the Association of Universities for Research in Astronomy, Inc., under NASA contract NAS 5-26555. These observations are associated with program No. 15115. Support for this work was provided by NASA through grant No. HST-GO-15115 from the Space Telescope Science Institute, which is operated by AURA, Inc., under NASA contract NAS 5-26555.

The authors thank the anonymous referee for helpful suggestions and comments that improved this paper. We acknowledge the importance of the conference “Particle Astrophysics and Cosmology Including Fundamental InteraCTIONS (PACIFIC-2013)” in

preparing for this program. We fully appreciate input from Luis Ho, Renyue Cen, Hyewon Suh, Takahiro Morishita, and Peter Williams. X.D., S.B., and T.T. acknowledge support by the Packard Foundation through a Packard Research fellowship to T.T. T.T. acknowledges support by NSF through grant AST-1412315. V.N.B. gratefully acknowledges assistance from a NASA grant associated with *HST* proposal GO 15215. J.S. is supported by JSPS KAKENHI grant No. JP18H01251 and the World Premier International Research Center Initiative (WPI), MEXT, Japan. A.S. is supported by the EACOA fellowship.

Software: LENSTRONOMY (Birrer & Amara 2018), ASTROPY (Astropy Collaboration et al. 2013), PHOTUTILS (Bradley et al. 2016), TOPCAT (Taylor 2005), MATPLOTLIB (Hunter 2007), and standard Python libraries.

Appendix A AGN Host Galaxy Luminosity with a Correction for Passive Evolution

In the passive evolution scenario, we expect the galaxy luminosity to fade over time. Thus, we transfer the L_{host} for distant samples to the value of today so as to compare the $\mathcal{M}_{\text{BH}}-L_{\text{host}}$ relation to the local in the equivalent frame. We consider this scenario following Ding et al. (2017b) by parameterizing the luminosity evolution with the functional form as

$$dmag_{\text{R}} \sim d \log(1+z), \text{ i.e.,}$$

$$\log(L_{R,0}) = \log(L_R) - 1.48 \log(1+z). \quad (10)$$

This formalism is more accurate when fit to the luminosity evolution with a broad range redshift compared to the fitting using a single slope formalism, i.e., $dmag/dz$. We refer interested readers to Ding et al. (2017b; Section 5.4) for more details.

Having transferred the L_{host} to today, we find that, as shown in Figure 14(a), at fixed mass, the black hole in the more distant universe tends to reside in less luminous hosts, which is consistent with the $\mathcal{M}_{\text{BH}}-M_*$ relation. Based on the 32 AGN systems, we fit the offset as a function of redshift in form as Equation (9) and obtain $\gamma = 1.07 \pm 0.23$, as shown in Figure 14(b). We further consider the selection effect using the previous approach as introduced in Section 5.5 and obtain $\gamma = 0.5 \pm 0.5$ and 0.6 ± 0.4 , with flat and lognormal priors, respectively, as shown in Figures 14(c) and (d).

The inferred γ here could have large systematics given the following limitations. First, the passive evolution is based on a simplified correction; after all, we are not clear exactly how the host evolves to $z=0$. Moreover, we only consider the evolution of the host galaxy and assume that \mathcal{M}_{BH} does not change much.

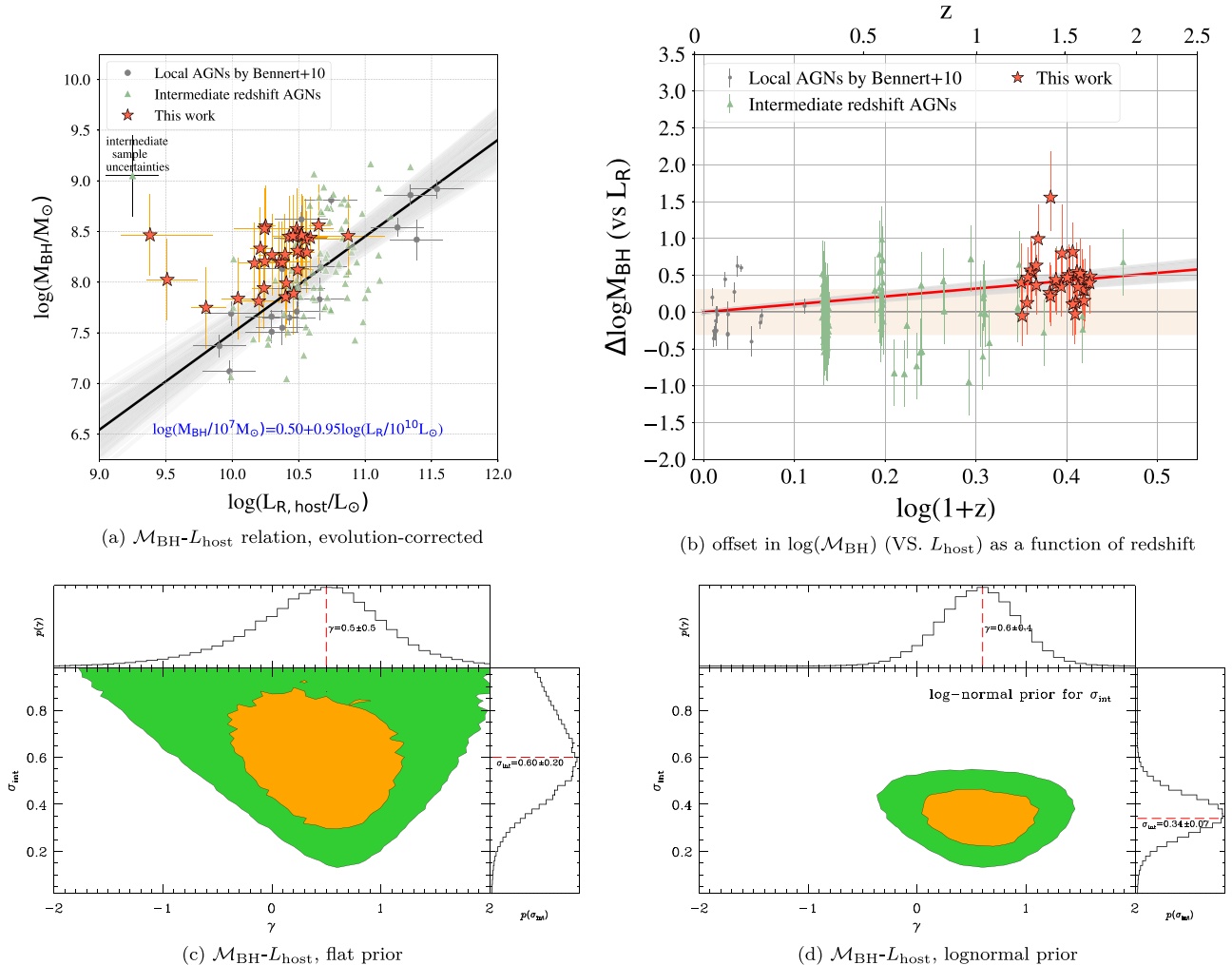


Figure 14. Same as previous figures but for the $\mathcal{M}_{\text{BH}}-L_{\text{host}}$ relation, considering the passive evolution correction for host galaxy luminosity.

Appendix B
The $\mathcal{M}_{\text{BH}}-M_*$ Comparison Sample

We use the self-consistent recipes to recalibrate the measurements of our comparison sample. We list the values of all of the comparison $\mathcal{M}_{\text{BH}}-M_*$ sample in Table 7.

Table 7
Data Summary for the Comparison $\mathcal{M}_{\text{BH}}-M_*$ Sample

Object ID ^a	z	$\log M_*$ (M_\odot)	$\log \mathcal{M}_{\text{BH}}$ (M_\odot)
Local Sample by Häring & Rix (2004)			
M87	0.0037 ^b	$11.78^c \pm 0.18$	9.48 ± 0.2
NGC 1068	0.0035	10.36 ± 0.18	7.15 ± 0.1
NGC 3379	0.0025	10.83 ± 0.18	8.00 ± 0.1
NGC 4374	0.0043	11.56 ± 0.18	8.63 ± 0.2
NGC 4261	0.0073	11.56 ± 0.18	8.72 ± 0.3
NGC 6251	0.0243	11.75 ± 0.18	8.72 ± 0.3
NGC 7052	0.0136	11.46 ± 0.18	8.52 ± 0.2
NGC 4742	0.0036	9.79 ± 0.18	7.15 ± 0.2
NGC 821	0.0056	11.11 ± 0.18	7.57 ± 0.2
IC 1459	0.0068	11.46 ± 0.18	9.40 ± 0.4
M31	0.0002	10.57 ± 0.18	7.65 ± 0.2
M32	0.0002	8.90 ± 0.18	6.40 ± 0.3
NGC 1023	0.0027	10.84 ± 0.18	7.64 ± 0.5
NGC 2778	0.0053	10.88 ± 0.18	7.15 ± 0.2
NGC 3115	0.0023	11.08 ± 0.18	9.00 ± 0.2
NGC 3245	0.0049	10.83 ± 0.18	8.32 ± 0.3
NGC 3377	0.0026	10.20 ± 0.18	8.00 ± 0.6
NGC 3384	0.0027	10.30 ± 0.18	7.20 ± 0.4
NGC 3608	0.0053	10.99 ± 0.18	8.28 ± 0.3
NGC 4291	0.0061	11.11 ± 0.18	8.49 ± 0.2
NGC 4342	0.0036	10.08 ± 0.18	8.48 ± 0.2
NGC 4473	0.0037	10.96 ± 0.18	8.04 ± 0.6
NGC 4564	0.0035	10.64 ± 0.18	7.75 ± 0.4
NGC 4594	0.0023	11.43 ± 0.18	9.00 ± 0.3
NGC 4649	0.0039	11.69 ± 0.18	9.30 ± 0.0
NGC 4697	0.0027	11.04 ± 0.18	8.23 ± 0.6
NGC 5845	0.0060	10.57 ± 0.18	8.38 ± 0.1
NGC 7332	0.0053	10.18 ± 0.18	7.11 ± 0.2
NGC 7457	0.0031	9.85 ± 0.18	6.54 ± 0.1
Milky Way	0.0000	10.04 ± 0.18	6.57 ± 0.2

Local Sample by Bennert et al. (2011a)

0121–0102	0.0540	10.12 ± 0.24	7.44 ± 0.4
0206–0017	0.0430	10.95 ± 0.23	8.01 ± 0.4
0353–0623	0.0760	10.33 ± 0.22	7.44 ± 0.4
0802+3104	0.0410	10.38 ± 0.23	7.17 ± 0.4
0846+2522	0.0510	10.50 ± 0.23	8.52 ± 0.4
1042+0414	0.0524	10.32 ± 0.23	6.98 ± 0.4
1043+1105	0.0475	9.83 ± 0.24	7.67 ± 0.4
1049+2451	0.0550	10.41 ± 0.23	7.84 ± 0.4
1101+1102	0.0355	10.33 ± 0.22	7.77 ± 0.4
1116+4123	0.0210	10.20 ± 0.22	7.37 ± 0.4
1144+3653	0.0380	10.26 ± 0.22	7.36 ± 0.4
1210+3820	0.0229	9.94 ± 0.24	7.50 ± 0.4
1250–0249	0.0470	10.14 ± 0.22	7.65 ± 0.4
1323+2701	0.0559	9.65 ± 0.22	6.98 ± 0.4
1355+3834	0.0501	10.11 ± 0.23	7.96 ± 0.4
1405–0259	0.0541	10.04 ± 0.23	7.08 ± 0.4
1419+0754	0.0558	10.73 ± 0.21	7.51 ± 0.4
1434+4839	0.0365	10.30 ± 0.24	7.48 ± 0.4
1535+5754	0.0304	10.24 ± 0.24	7.83 ± 0.4
1545+1709	0.0481	9.92 ± 0.22	7.28 ± 0.4
1554+3238	0.0483	10.00 ± 0.23	7.63 ± 0.4
1557+0830	0.0465	9.82 ± 0.23	7.55 ± 0.4

Table 7
(Continued)

Object ID ^a	z	$\log M_*$ (M_\odot)	$\log \mathcal{M}_{\text{BH}}$ (M_\odot)
1605+3305	0.0532	9.95 ± 0.23	7.78 ± 0.4
1606+3324	0.0585	10.33 ± 0.22	7.22 ± 0.4
1611+5211	0.0409	10.33 ± 0.22	7.34 ± 0.4

Object ID	z	$\log M_*$ (M_\odot)	$\log \mathcal{M}_{\text{BH}}$ (M_\odot)
Intermediate Sample by Bennert et al. (2011b)			
J033252–275119	1.227	$10.58(9.83)^d \pm 0.2$	8.87 ± 0.4
J033243–274914	1.900	$10.64(10.64) \pm 0.2$	9.17 ± 0.4
J033239–274601	1.220	$10.54(10.54) \pm 0.2$	8.24 ± 0.4
J033226–274035	1.031	$10.78(9.53) \pm 0.2$	7.85 ± 0.4
J033225–274218	1.617	$10.61(10.61) \pm 0.2$	8.08 ± 0.4
J033210–274414	1.615	$10.45(10.45) \pm 0.2$	8.30 ± 0.4
J033200–274319	1.037	$9.62(9.62) \pm 0.2$	7.75 ± 0.4
J033229–274529	1.218	$10.71(10.71) \pm 0.2$	8.37 ± 0.4
J123553+621037	1.371	$10.90(9.99) \pm 0.2$	8.27 ± 0.4
J123618+621115	1.021	$10.96(9.29) \pm 0.2$	8.35 ± 0.4
J123707+622147	1.450	$10.74(10.74) \pm 0.2$	8.77 ± 0.4

Intermediate Sample by Schramm & Silverman (2013)

158	0.717	$10.66(10.66) \pm 0.2$	6.94 ± 0.4
170	1.065	$9.80(9.50) \pm 0.2$	6.84 ± 0.4
271	0.960	$10.49(9.85) \pm 0.2$	7.12 ± 0.4
273	0.970	$10.29(10.29) \pm 0.2$	7.99 ± 0.4
305	0.544	$11.01(11.01) \pm 0.2$	8.38 ± 0.4
333	1.044	$10.33(9.87) \pm 0.2$	7.66 ± 0.4
339	0.675	$10.96(10.96) \pm 0.2$	7.60 ± 0.4
348	0.569	$10.55(10.15) \pm 0.2$	7.64 ± 0.4
379	0.737	$10.66(10.17) \pm 0.2$	8.90 ± 0.4
413	0.664	$10.19(9.80) \pm 0.2$	6.81 ± 0.4
417	0.837	$10.39(9.91) \pm 0.2$	8.11 ± 0.4
465	0.740	$10.76(10.14) \pm 0.2$	7.78 ± 0.4
516	0.733	$10.88(10.71) \pm 0.2$	7.66 ± 0.4
540	0.622	$10.88(10.57) \pm 0.2$	7.38 ± 0.4
597	1.034	$10.91(10.80) \pm 0.2$	7.87 ± 0.4
712	0.841	$11.34(11.19) \pm 0.2$	8.41 ± 0.4

Intermediate Sample by Cisternas et al. (2011)

J095817.54+021938.5	0.73	10.30 ± 0.2	7.72 ± 0.4
J095819.88+022903.6	0.34	11.23 ± 0.2	8.29 ± 0.4
J095831.65+024901.6	0.34	10.65 ± 0.2	8.08 ± 0.4
J095840.61+020426.6	0.34	11.02 ± 0.2	8.39 ± 0.4
J095845.80+024634.0	0.35	10.54 ± 0.2	7.39 ± 0.4
J095902.76+021906.5	0.34	11.14 ± 0.2	8.66 ± 0.4
J095909.53+021916.5	0.38	10.68 ± 0.2	7.77 ± 0.4
J095928.31+022106.9	0.35	10.95 ± 0.2	7.24 ± 0.4
J100002.21+021631.8	0.85	11.07 ± 0.2	8.29 ± 0.4
J100012.91+023522.8	0.70	11.17 ± 0.2	8.15 ± 0.4
J100014.55+023852.7	0.44	10.57 ± 0.2	7.79 ± 0.4
J100017.54+020012.6	0.35	10.47 ± 0.2	7.59 ± 0.4
J100025.25+015852.2	0.37	10.57 ± 0.2	8.58 ± 0.4
J100028.63+025112.7	0.77	10.86 ± 0.2	8.49 ± 0.4
J100029.69+022129.7	0.73	11.01 ± 0.2	8.03 ± 0.4
J100033.38+015237.2	0.83	10.81 ± 0.2	8.07 ± 0.4
J100033.49+013811.6	0.52	10.54 ± 0.2	8.01 ± 0.4
J100037.29+024950.6	0.73	10.36 ± 0.2	7.41 ± 0.4
J100043.15+020637.2	0.36	11.28 ± 0.2	8.07 ± 0.4
J100046.72+020404.5	0.55	11.08 ± 0.2	7.75 ± 0.4
J100058.71+022556.2	0.69	10.66 ± 0.2	7.91 ± 0.4
J100118.52+015543.0	0.53	10.84 ± 0.2	8.22 ± 0.4
J100141.09+021300.0	0.62	10.53 ± 0.2	7.35 ± 0.4













Table 7
(Continued)

Object ID	z	$\log M_*$ (M_\odot)	$\log \mathcal{M}_{\text{BH}}$ (M_\odot)
J100146.49+020256.7	0.67	10.75 ± 0.2	7.73 ± 0.4
J100202.22+024157.8	0.79	10.53 ± 0.2	8.24 ± 0.4
J100205.03+023731.5	0.52	11.15 ± 0.2	8.38 ± 0.4
J100212.11+014232.4	0.37	10.48 ± 0.2	7.70 ± 0.4
J100218.32+021053.1	0.55	11.20 ± 0.2	8.61 ± 0.4
J100230.06+014810.4	0.63	10.73 ± 0.2	7.50 ± 0.4
J100230.65+024427.6	0.82	10.77 ± 0.2	7.82 ± 0.4
J100232.13+023537.3	0.66	11.03 ± 0.2	8.19 ± 0.4
J100243.96+023428.6	0.38	11.08 ± 0.2	8.25 ± 0.4

Notes.

- ^a The object name is directly adopted from the reference.
^b For the Häring & Rix (2004) sample, the redshift value is calculated from the Galaxy distance, assuming a perfect Hubble flow.
^c The M_* for the local sample is the bulge mass.
^d If applicable, the values in brackets are the bulge mass.

ORCID iDs

- Xuheng Ding  <https://orcid.org/0000-0001-8917-2148>
 John Silverman  <https://orcid.org/0000-0002-0000-6977>
 Tommaso Treu  <https://orcid.org/0000-0002-8460-0390>
 Andreas Schulze  <https://orcid.org/0000-0002-6660-6131>
 Simon Birrer  <https://orcid.org/0000-0003-3195-5507>
 Daeseong Park  <https://orcid.org/0000-0001-9877-1732>
 Knud Jahnke  <https://orcid.org/0000-0003-3804-2137>
 Vardha N. Bennert  <https://orcid.org/0000-0003-2064-0518>
 Jeyhan S. Kartaltepe  <https://orcid.org/0000-0001-9187-3605>
 Anton M. Koekemoer  <https://orcid.org/0000-0002-6610-2048>
 Matthew A. Malkan  <https://orcid.org/0000-0001-6919-1237>
 David Sanders  <https://orcid.org/0000-0002-1233-9998>

References

Astropy Collaboration, Robitaille, T. P., Tollerud, E. J., et al. 2013, *A&A*, **558**, A33
 Baskin, A., & Laor, A. 2005, *MNRAS*, **356**, 1029
 Beifiori, A., Courteau, S., Corsini, E. M., & Zhu, Y. 2012, *MNRAS*, **419**, 2497
 Bell, E. F., & de Jong, R. S. 2000, *MNRAS*, **312**, 497
 Bell, E. F., & de Jong, R. S. 2001, *ApJ*, **550**, 212
 Bennert, V. N., Auger, M. W., Treu, T., Woo, J.-H., & Malkan, M. A. 2011a, *ApJ*, **726**, 59
 Bennert, V. N., Auger, M. W., Treu, T., Woo, J.-H., & Malkan, M. A. 2011b, *ApJ*, **742**, 107
 Bennert, V. N., Treu, T., Auger, M. W., et al. 2015, *ApJ*, **809**, 20
 Bennert, V. N., Treu, T., Woo, J., et al. 2010, *ApJ*, **708**, 1507
 Bentz, M. C., & Manne-Nicholas, E. 2018, *ApJ*, **864**, 146
 Birrer, S., & Amara, A. 2018, *PDU*, **22**, 189
 Birrer, S., Amara, A., & Refregier, A. 2015, *ApJ*, **813**, 102
 Birrer, S., Treu, T., Rusu, C. E., et al. 2019, *MNRAS*, **484**, 4726
 Blanton, M. R., & Roweis, S. 2007, *AJ*, **133**, 734
 Bradley, L., Sipocz, B., Robitaille, T., et al. 2016, *astropy/photutils v0.3*, Zenodo, doi:10.5281/zenodo.164986
 Brammer, G. B., van Dokkum, P. G., Franx, M., et al. 2012, *ApJS*, **200**, 13
 Bruce, V. A., Dunlop, J. S., McLure, R. J., et al. 2014, *MNRAS*, **444**, 1660
 Bruzual, G., & Charlot, S. 2003, *MNRAS*, **344**, 1000
 Cen, R. 2015, *ApJL*, **805**, L9
 Chen, G. C.-F., Suyu, S. H., Wong, K. C., et al. 2016, *MNRAS*, **462**, 3457
 Cisternas, M., Jahnke, K., Bongiorno, A., et al. 2011, *ApJL*, **741**, L11
 Civano, F., Marchesi, S., Comastri, A., et al. 2016, *ApJ*, **819**, 62

Decarli, R., Falomo, R., Treves, A., et al. 2010, *MNRAS*, **402**, 2441
 DeGraf, C., Di Matteo, T., Treu, T., et al. 2015, *MNRAS*, **454**, 913
 Di Matteo, T., Colberg, J., Springel, V., Hernquist, L., & Sijacki, D. 2008, *ApJ*, **676**, 33
 Dimauro, P., Huertas-Company, M., Daddi, E., et al. 2018, *MNRAS*, **478**, 5410
 Ding, X., Liao, K., Treu, T., et al. 2017a, *MNRAS*, **465**, 4634
 Ding, X., Treu, T., Suyu, S. H., et al. 2017b, *MNRAS*, **472**, 90
 Ferrarese, L., & Merritt, D. 2000, *ApJL*, **539**, L9
 Gallazzi, A., & Bell, E. F. 2009, *ApJS*, **185**, 253
 Gebhardt, K., Bender, R., Bower, G., et al. 2001, *ApJL*, **555**, L75
 Graham, A. W., Onken, C. A., Athanassoula, E., & Combes, F. 2011, *MNRAS*, **412**, 2211
 Greene, J. E., & Ho, L. C. 2005, *ApJ*, **630**, 122
 Groggin, N. A., Kocevski, D. D., Faber, S. M., et al. 2011, *ApJS*, **197**, 35
 Gültekin, K., Richstone, D. O., Gebhardt, K., et al. 2009, *ApJ*, **698**, 198
 Häring, N., & Rix, H.-W. 2004, *ApJL*, **604**, L89
 Harris, C. E., Bennert, V. N., Auger, M. W., et al. 2012, *ApJS*, **201**, 29
 Hirschmann, M., Khochfar, S., Burkert, A., et al. 2010, *MNRAS*, **407**, 1016
 Hopkins, P. F., Hernquist, L., Cox, T. J., & Kereš, D. 2008, *ApJS*, **175**, 356
 Hunter, J. D. 2007, *CSE*, **9**, 90
 Jahnke, K., Bongiorno, A., Brusa, M., et al. 2009, *ApJL*, **706**, L215
 Jahnke, K., & Macciò, A. V. 2011, *ApJ*, **734**, 92
 Kennedy, J., & Eberhart, R. 1995, in Proc. Int. Conf. Neural Networks 4 (Piscataway, NJ: IEEE), 1942, doi:10.1109/ICNN.1995.488968
 Kim, M., Ho, L. C., Peng, C. Y., Barth, A. J., & Im, M. 2008, *ApJS*, **179**, 283
 Kimura, M., Maihara, T., Iwamuro, F., et al. 2010, *PASJ*, **62**, 1135
 Koekemoer, A. M., Aussel, H., Calzetti, D., et al. 2007, *ApJS*, **172**, 196
 Koekemoer, A. M., Faber, S. M., Ferguson, H. C., et al. 2011, *ApJS*, **197**, 36
 Kormendy, J., & Ho, L. C. 2013, *ARA&A*, **51**, 511
 Laigle, C., McCracken, H. J., Ilbert, O., et al. 2016, *ApJS*, **224**, 24
 Lauer, T. R., Tremaine, S., Richstone, D., & Faber, S. M. 2007, *ApJ*, **670**, 249
 Lehmer, B. D., Brandt, W. N., Alexander, D. M., et al. 2005, *ApJS*, **161**, 21
 Magorrian, J., Tremaine, S., Richstone, D., et al. 1998, *AJ*, **115**, 2285
 Marconi, A., & Hunt, L. K. 2003, *ApJL*, **589**, L21
 Matsuoka, K., Silverman, J. D., Schramm, M., et al. 2013, *ApJ*, **771**, 64
 McLure, R. J., & Dunlop, J. S. 2004, *MNRAS*, **352**, 1390
 Mechtley, M., Jahnke, K., Windhorst, R. A., et al. 2016, *ApJ*, **830**, 156
 Mechtley, M., Windhorst, R. A., Ryan, R. E., et al. 2012, *ApJL*, **756**, L38
 Menci, N., Fiore, F., Bongiorno, A., & Lamastra, A. 2016, *A&A*, **594**, A99
 Merloni, A., Bongiorno, A., Bolzonella, M., et al. 2010, *ApJ*, **708**, 137
 Momcheva, I. G., Brammer, G. B., van Dokkum, P. G., et al. 2016, *ApJS*, **225**, 27
 Nobuta, K., Akiyama, M., Ueda, Y., et al. 2012, *ApJ*, **761**, 143
 Park, D., Woo, J.-H., Bennert, V. N., et al. 2015, *ApJ*, **799**, 164
 Peng, C. Y. 2007, *ApJ*, **671**, 1098
 Peng, C. Y., Impey, C. D., Ho, L. C., Barton, E. J., & Rix, H.-W. 2006a, *ApJ*, **640**, 114
 Peng, C. Y., Impey, C. D., Rix, H.-W., et al. 2006b, *ApJ*, **649**, 616
 Peterson, B. M., Ferrarese, L., Gilbert, K. M., et al. 2004, *ApJ*, **613**, 682
 Salvander, S., Shields, G. A., Gebhardt, K., & Bonning, E. W. 2006, *NewAR*, **50**, 803
 Schramm, M., & Silverman, J. D. 2013, *ApJ*, **767**, 13
 Schulze, A., Bongiorno, A., Gavignaud, I., et al. 2015, *MNRAS*, **447**, 2085
 Schulze, A., Silverman, J. D., Kashino, D., et al. 2018, *ApJS*, **239**, 22
 Schulze, A., & Wisotzki, L. 2011, *A&A*, **535**, A87
 Schulze, A., & Wisotzki, L. 2014, *MNRAS*, **438**, 3422
 Scoville, N., Abraham, R. G., Aussel, H., et al. 2007, *ApJS*, **172**, 38
 Shen, Y. 2013, *BASI*, **41**, 61
 Springel, V., White, S. D. M., Jenkins, A., et al. 2005, *Natur*, **435**, 629
 Suh, H., Hasinger, G., Steinhardt, C., Silverman, J. D., & Schramm, M. 2015, *ApJ*, **815**, 129
 Sun, M., Trump, J. R., Brandt, W. N., et al. 2015, *ApJ*, **802**, 14
 Taylor, M. B. 2005, in ASP Conf. Ser. 347, *Astronomical Data Analysis Software and Systems XIV*, ed. P. Shopbell, M. Britton, & R. Ebert (San Francisco, CA: ASP), 29
 Trakhtenbrot, B., & Netzer, H. 2012, *MNRAS*, **427**, 3081
 Treu, T., Malkan, M. A., & Blandford, R. D. 2004, *ApJL*, **615**, L97
 Treu, T., Woo, J.-H., Malkan, M. A., & Blandford, R. D. 2007, *ApJ*, **667**, 117
 Ueda, Y., Watson, M. G., Stewart, I. M., et al. 2008, *ApJS*, **179**, 124
 van der Wel, A., Bell, E. F., Häussler, B., et al. 2012, *ApJS*, **203**, 24
 Vestergaard, M., & Peterson, B. M. 2006, *ApJ*, **641**, 689
 Woo, J., Treu, T., Malkan, M. A., & Blandford, R. D. 2006, *ApJ*, **645**, 900
 Woo, J.-H., Treu, T., Barth, A. J., et al. 2010, *ApJ*, **716**, 269
 Woo, J.-H., Treu, T., Malkan, M. A., & Blandford, R. D. 2008, *ApJ*, **681**, 925
 Xue, Y. Q., Luo, B., Brandt, W. N., et al. 2011, *ApJS*, **195**, 10